

# Searches for stochastic gravitational-wave backgrounds

Joseph D. Romano

Les Houches Summer School  
July 2018

## Abstract

These lecture notes provide a brief introduction to methods used to search for a stochastic background of gravitational radiation—a superposition of gravitational-wave signals that are either too weak or too numerous to individually detect. The lectures are divided into two parts: (i) an overview, consisting of a description of different types of gravitational-wave backgrounds and an introduction to the method of cross-correlating data from multiple detectors to extract signal from noise; (ii) details, extending the previous discussion to non-trivial detector response, what to do in the absence of correlations, and a recently proposed Bayesian method to search for the gravitational-wave background produced by stellar-mass binary black hole mergers throughout the universe. Suggested exercises for the reader are given throughout the text.

# Contents

<b>I Overview / Basics</b>	<b>4</b>
<b>1 Motivation</b>	<b>4</b>
1.1 Gravitational-wave analogue of the cosmic microwave background . . . . .	4
1.2 The background of BBH and BNS mergers in the LIGO band . . . . .	5
<b>2 Different types of stochastic backgrounds</b>	<b>7</b>
2.1 Different sources . . . . .	7
2.2 Different signal properties . . . . .	8
<b>3 Mathematical characterization of a stochastic background</b>	<b>11</b>
3.1 Plane-wave expansion . . . . .	11
3.2 Ensemble averages . . . . .	12
3.3 Energy density spectrum in gravitational waves . . . . .	13
3.4 Calculating $\Omega_{\text{gw}}(f)$ for an astrophysically-generated background . . . . .	14
3.4.1 Example: $\Omega_{\text{gw}}(f)$ for binary inspiral . . . . .	14
<b>4 Correlation methods</b>	<b>16</b>
4.1 Basic idea . . . . .	16
4.2 Extension to multiple data samples . . . . .	17
4.3 Optimal filtering . . . . .	18
<b>5 Optimal filtering applied to some simple examples</b>	<b>19</b>
5.1 Single-component analyses . . . . .	21
5.2 Multi-component analysis . . . . .	21
<b>II Details / Examples</b>	<b>22</b>
<b>6 Non-trivial detector response</b>	<b>23</b>
6.1 Beam detectors and different types of detector response . . . . .	23
6.2 Detector response functions . . . . .	24
6.3 Examples . . . . .	24
6.3.1 Detector response for a one-arm, one-way detector . . . . .	24
6.3.2 Detector response for a laser interferometer in the short-antenna limit . . . . .	26
<b>7 Non-trivial correlations</b>	<b>27</b>
7.1 Overlap function . . . . .	27
7.2 Examples . . . . .	28
7.2.1 Overlap function for a pair of laser interferometers in the short-antenna limit	28
7.2.2 Overlap function for pulsar timing arrays . . . . .	28
7.2.3 Overlap function for a pair of electric dipole antennas . . . . .	29
<b>8 What to do in the absence of correlations?</b>	<b>30</b>
<b>9 Frequentist statistics and Bayesian inference</b>	<b>31</b>

10 Searching for the background of binary black-hole mergers	32
11 Exercises	35

DRAFT

# Part I

## Overview / Basics

In the first part of these notes, we describe different types of stochastic gravitational-wave backgrounds and introduce the method of cross-correlation for extracting the signal from noise.

### 1 Motivation

A stochastic background of gravitational radiation is a superposition of gravitational-wave signals that are either too weak or too numerous to individually detect. The individual signals making up the background are thus *unresolvable*, unlike the large signal-to-noise binary black-hole (BBH) and binary neutron-star (BNS) merger signals recently detected by the advanced LIGO and Virgo detectors. But despite the fact that the individual signals are unresolvable, the detection of a gravitational-wave background (GWB) will provide information about the *statistical* properties (or population properties) of the source.

#### 1.1 Gravitational-wave analogue of the cosmic microwave background

The ultimate goal of GWB searches is to produce the GW analogue of Figure 1, which is a sky map

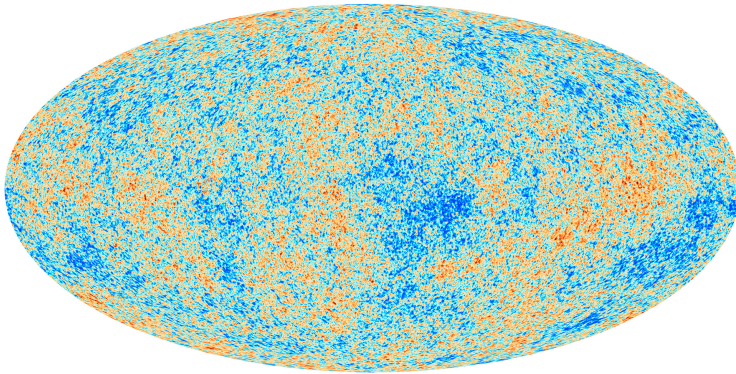


Figure 1: Skymap of  $\Delta T/T_0$  for the cosmic microwave background radiation produced by the Planck 2013 mission.

of the temperature fluctuations in the cosmic microwave background (CMB) blackbody radiation,  $\Delta T/T_0$ , relative to the  $T_0 = 2.73$  K isotropic component. (The dipole contribution due to our motion with respect to the cosmic rest frame has also been subtracted out.) The CMB is a background of electromagnetic radiation, produced roughly 380,000 yr after the Big Bang. At that time, the universe had a temperature of  $\sim 3000$  K, approximately one thousand times larger than the temperature today, but cool enough for neutral hydrogen atoms to first form and photons to propagate freely. The temperature fluctuations in the CMB radiation tell us about the density perturbations at the time of last scattering of photons, thus giving us a picture of the “seeds” of large-scale structure formation in the early universe. Given the weakness of the gravitational interaction compared to the electromagnetic force, the GW analogue of Figure 1 would provide information about a much earlier time in the evolution of the universe, a mere fraction of a second

after the Big Bang (this is explained in a bit more detail in Section 2.1). Detecting the cosmological GWB is thus a “holy grail” for GW astronomy.

For perspective, Figure 1 was produced by the Planck mission in 2013, almost 50 years after the CMB radiation was initially detected by Penzias and Wilson in 1965. It took many years and improved experiments (COBE, Boomerang, WMAP, Planck to name a few) to get to the high-precision measurements that we have today. So it is somewhat sobering to realize that now—at the end of 2018—we have yet to detect the isotropic component of the GWB.

## 1.2 The background of BBH and BNS mergers in the LIGO band

Even though a detailed map of the primordial GWB is likely to be out of reach for many years, there are other sources of GWBs that are much more immediately accessible to us. For example, as mentioned above, the advanced LIGO and Virgo detectors have detected other gravitational-wave signals from several individual BBH and BNS mergers. These were very strong signals, having matched-filter signal-to-noise ratios (SNR)  $\gtrsim 10$ , and false alarm probabilities  $< 2 \times 10^{-7}$ , corresponding to 5-sigma “gold-plated” events. Similar large-SNR detections are expected during the observing run O3, which started on 1 April 2019. But we also expect that there are many more signals, corresponding to more distant mergers or smaller mass systems, which are individually undetectable (i.e., *subthreshold* events). This weaker background of gravitational radiation is nonetheless detectable as a combined/aggregate signal via the common influence of the component GWs on multiple detectors.

To get an idea of the statistical properties of this background signal, we can estimate the total rate of stellar-mass BBH mergers throughout the universe by using the local rate estimate from these first detections,  $9\text{--}240 \text{ Gpc}^{-3} \text{ yr}^{-1}$ . This leads to a prediction for the total rate of BBH mergers between  $\sim 1$  per minute to a few per hour. (You are asked in Exercise 1 to verify these predictions.)<sup>1</sup> Since the duration of BBH merger signals in band is  $\sim 1$  s, which is much smaller than the average duration between successive mergers, the combined signal will consist of discrete bursts of radiation separated by periods of silence (i.e., it will be *popcorn-like*). We can perform similar calculations for BNS mergers. The predicted total rate for such events is roughly one event every 15 s, while the duration of a BNS signal in band is roughly 100 s. Thus, the BNS merger signals overlap in time leading to a continuous (or *confusion-limited*) background. Figure 2 is a plot of the expected time-domain signal corresponding to the rate estimates mentioned above.

The combined signal from BBH and BNS mergers is potentially detectable with advanced LIGO and Virgo, shortly after reaching design sensitivity. Although the signal-to-noise ratios for the individual events are small, the combined signal-to-noise ratio of the correlated data summed over all events grows like the square-root of the observation time, reaching a detectable level of 3-sigma after roughly 40 months of observation (Figure 3). This estimate of time to detection is based on the standard cross-correlation search (Section 4), which assumes a Gaussian-stationary background. But there is a new method, recently proposed by Smith and Thrane [3], which can potentially reduce the time to detection by several orders of magnitude (factor of  $\sim 1000$ ), meaning that the background would be detectable after only a few days of operation. We will describe this method in more detail in Section 10.

---

<sup>1</sup>A more complete description of this and all other exercises are given in Section 11. The number next to “Exercise” is a link that brings you to the detailed exercise in Section 11.

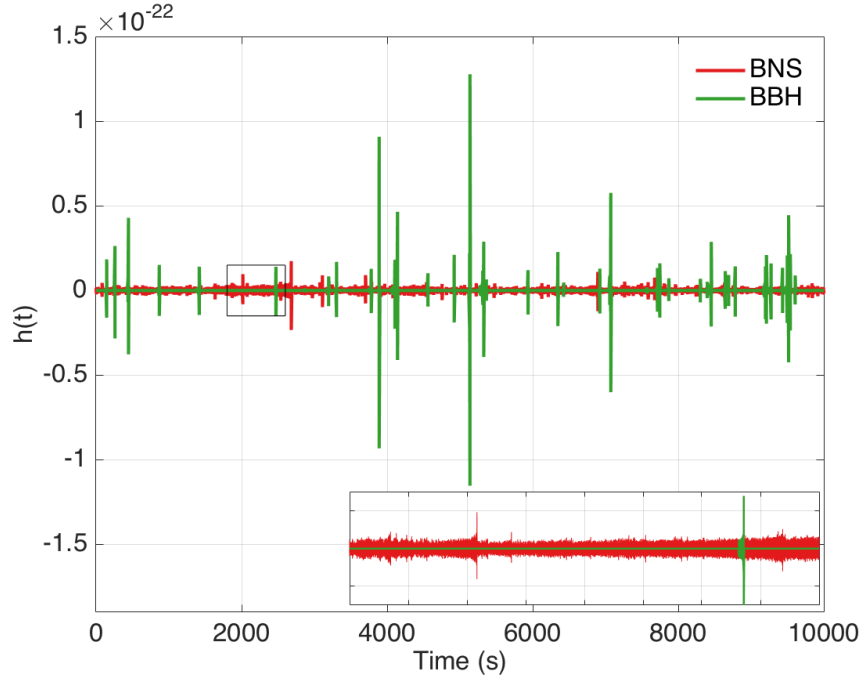


Figure 2: Simulated time-domain signal for the predicted BBH and BNS background. Figure taken from [?].

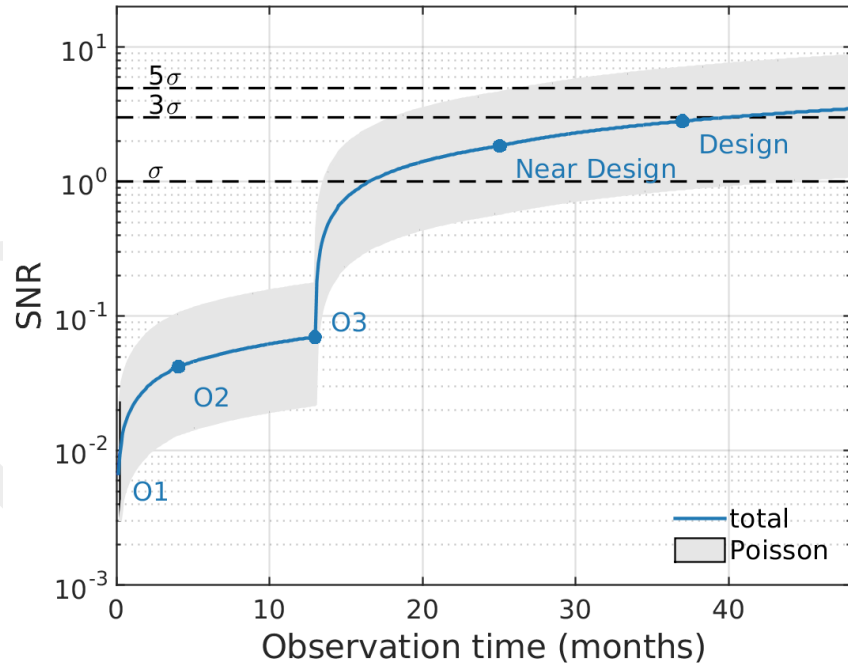


Figure 3: Expected signal-to-noise ratio of the correlated data for the advanced LIGO and Virgo detectors as a function of observation time. The points labeled O1, O2, etc., indicate the start of advanced LIGO's first observation run, second observation run, etc. Figure taken from [?].

## 2 Different types of stochastic backgrounds

### 2.1 Different sources

The combined signal from stellar-mass BBH and BNS mergers throughout the universe is just one way of producing a GWB. Due to the relatively small masses of stellar-mass BHs and NSs, the signal is at the high-frequency end of the spectrum ( $\sim 10$  Hz to a few kHz), which is the sensitive band for the current generation of km-scale ground-based laser interferometers like LIGO and Virgo. Heavier-mass systems, which produce lower-frequency gravitational waves, are also expected to give rise to GWBs that are potentially detectable with other existing or proposed detectors. Figure 4 is a plot of the GW spectrum, with frequencies ranging from a few kHz (for ground-based detectors) to  $10^{-17}$  Hz (corresponding to a period equal to the age of the universe), together with potential sources of GWBs and relevant detectors.

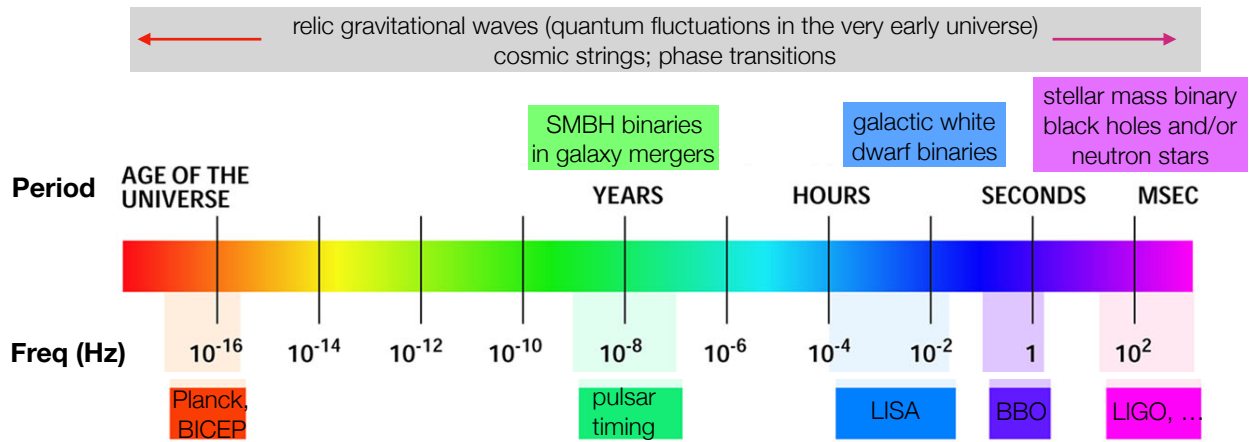


Figure 4: Detectors and potential sources of GWBs across the GW spectrum. Note that the GWB signal from cosmic strings and phase transitions stretch across a broad range of frequencies, and peak at basically any frequency depending on the parameters that define the string network and the energy scale where the phase transition occurs. Also, the primordial background of relic GWs predicted by standard inflation is flat across the whole frequency band shown here.

Of particular note is the combined GW signal produced by compact white-dwarf binaries in the Milky Way, producing a “confusion-limited” GWB in the frequency band  $\sim 10^{-4}$  Hz to  $10^{-1}$  Hz. This is a guaranteed signal for the proposed space-based interferometer LISA (expected launch date 2034), which consists of three spacecraft in an equilateral-triangle configuration in orbit around the Sun. Each spacecraft houses two lasers, two telescopes, and two test masses; the arms will be several million km long. The confusion-limited white-dwarf binary signal is expected to be so strong that it will dominate the instrumental noise at low frequencies, forming a GW “foreground” that will have to be contended with when searching for other gravitational sources in the LISA band.

At lower frequencies between  $\sim 10^{-9}$  Hz and  $10^{-7}$  Hz (corresponding to periods of order decades to years), pulsar timing arrays can be used to search for the GWB produced by the inspiral and merger of supermassive black-holes (SMBHs) in the centers of distant galaxies. A pulsar timing array basically functions as a galactic-scale gravitational-wave detector, with the radio pulses emitted by each pulsar behaving like ‘ticks’ of an extremely stable clock. By carefully monitoring the

arrival times of these radio pulses, one can search for a GWB by looking for correlated modulations in the arrival times induced by a passing gravitational wave.

In addition to these *astrophysical* GWBs associated with stellar-mass or supermassive BHs and NSs, one also expects backgrounds of *cosmological* origin, produced in the very early universe, much before the formation of stars and galaxies. Two examples, indicated in Figure 4, are cosmic strings (line-like topological defects associated with phase transitions in the early universe) and relic gravitational waves (quantum fluctuations in the geometry of space-time, driven to macroscopic scales by a period of rapid expansion—e.g., inflation—a mere  $\sim 10^{-32}$  s after the Big Bang). This relic background is potentially detectable by its effect on the polarization of the CMB radiation. This signal has been searched for by CMB experiments such as Planck and BICEP, and is a core target of many proposed future experiments, such as PIXIE and LiteBIRD.

## 2.2 Different signal properties

Not surprisingly, different sources of a GWB give rise, in general, to different properties of the observed signal. These differences are what will allow us to infer the source of the background from the measured signal.

(i) Stochastic backgrounds can differ from one another in terms of the angular distribution of gravitational-wave power on the sky. Cosmologically-generated backgrounds, like those from cosmic strings or relic GWs, are expected to be *statistically isotropic*, qualitatively similar to the CMB (Figure 1). The GW power in these backgrounds is *anisotropic*, following the spatial distribution of the particular sources that produced it, but has no preferred direction when averaged over different realizations of the sources. Different statistically isotropic backgrounds will be characterized by different angular power spectra,  $C_l$  as a function of multipole moment  $l$ , where

$$C(\theta) = \sum_{l=0}^{\infty} \frac{2l+1}{4\pi} C_l P_l(\cos \theta), \quad (2.1)$$

is the angular correlation between the GW power coming from two directions  $\hat{n}$  and  $\hat{n}'$  separated by angle  $\theta$ . If all of the  $C_l$ 's except the monopole,  $C_0$ , are equal to zero, then the GWB is said to be “exactly” isotropic. Exact isotropy is the simplest mathematical model for stochastic backgrounds, and will be discussed further in Section 3.2.

Statistically isotropic backgrounds are to be contrasted with *statistically anisotropic* backgrounds, whose distribution of power on the sky has preferred directions, even when averaged over different realizations of the sources that produce it. For example, the “confusion-limited” foreground that LISA will see from the population of close white-dwarf binaries in the Milky Way will have its GW power concentrated in the direction of the Milky Way. Figure 5 shows simulated skymaps for a statistically isotropic background (left panel) and a statistically anisotropic background (right panel). The anisotropic background in that figure follows the galactic plane in equatorial coordinates.

(ii) Stochastic backgrounds can also differ from one another in temporal distribution and amplitude. We have already seen examples of this in Figure 2, for the expected backgrounds from stellar-mass BBH mergers and BNS mergers throughout the universe (a LIGO source). As mentioned earlier, the rate estimates and durations of these individual merger signals are such that the BBH background is expected to be popcorn-like (consisting of non-overlapping mergers), while that for the BNS background is expected to be stationary and confusion-limited (consisting of several overlapping BNS mergers at any instant of time). Another example of non-trivial temporal dependence is the confusion-limited signal from close white-dwarf binaries in the Milky Way (a LISA

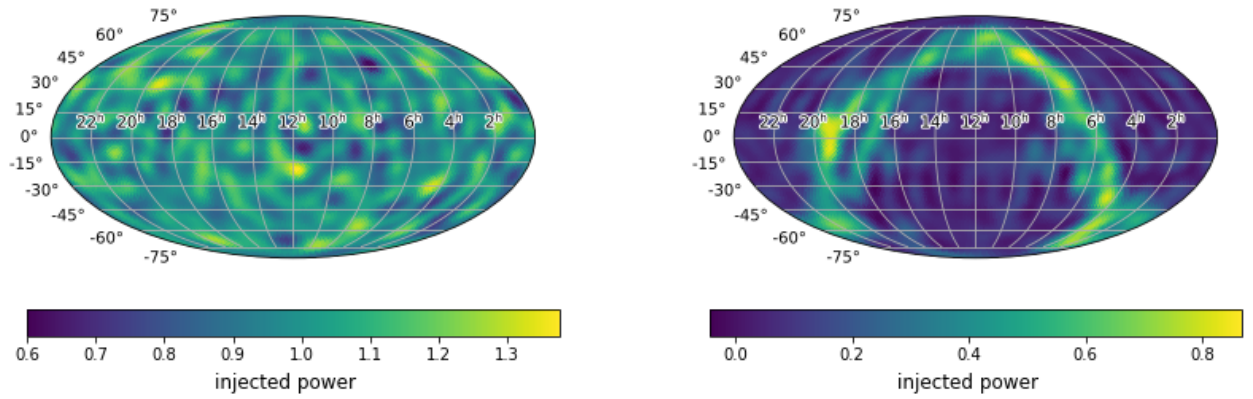


Figure 5: Simulated sky maps of gravitational-wave power for a statistically isotropic background (left panel) and an anisotropic background (right panel).

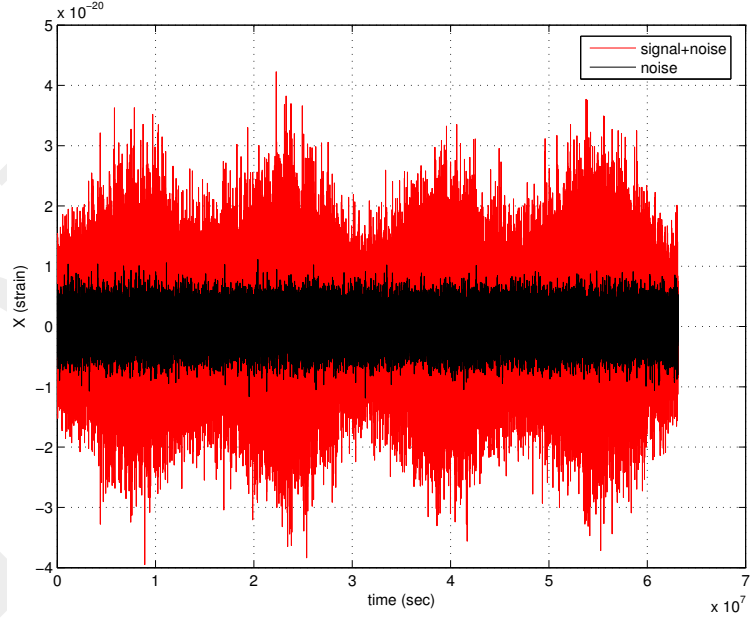


Figure 6: Simulated time-domain output of a particular combination of the LISA data over a 2-year period. The modulation of the signal with a 6-month period is apparent in the data. Figure taken from [2].

source). This is an amplitude-modulated signal with a 6-month period (Figure 6), due to LISA’s “cartwheeling” orbital motion around the Sun. (The antenna pattern of LISA will point in the direction of the Galactic center twice every year.) From the figure, we also see that the expected white-dwarf binary signal will be larger than that of the instrumental noise for LISA, thus constituting an astrophysical *foreground*. This is atypical, however, as most expected GWBs will sit below the instrumental noise (e.g., for advanced LIGO / Virgo, pulsar timing, CMB polarization experiments), requiring observation over long periods of time to confidently detect.

(iii) Stochastic backgrounds can also differ in their power spectra<sup>2</sup> as shown in Figure 7. Here

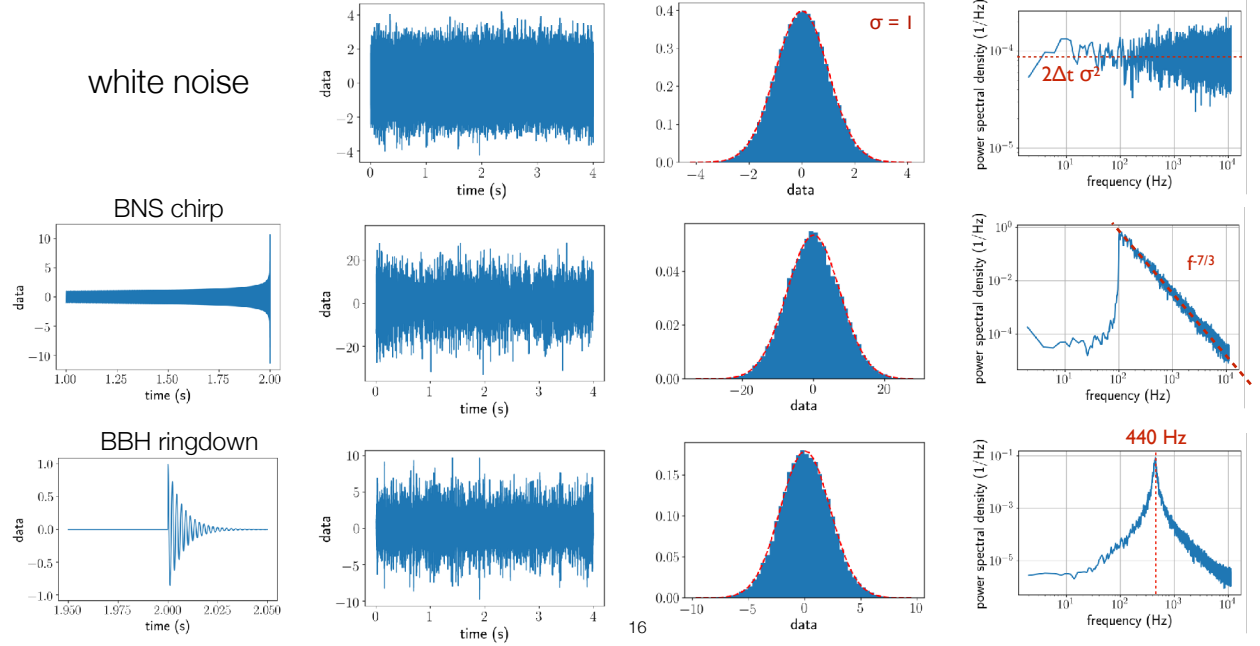


Figure 7: Simulated time-domain data (including the signals for an individual BNS merger and BBH ringdown), histograms, and power spectra for three different types of Gaussian-stationary GWBs.

we plot simulated time-domain data (including the signals for an individual BNS merger and BBH ringdown<sup>3</sup>), histograms, and power spectra for three different types of GWBs. For these toy-model simulations, we overlapped a sufficient number of individual BNS merger and BBH ringdown signals to produce Gaussian-stationary confusion-limited GWBs (second and third columns). The difference between these backgrounds shows up in their power spectra (third column). The power spectra for the BNS merger and BBH ringdown backgrounds have the same shape as those for an individual BNS merger or BBH ringdown, scaled by the total number of sources contributing to the background.

<sup>2</sup>Recall that if  $x(t)$  is stationary time-domain data, then the power spectrum  $P_x(f)$  is defined as the Fourier transform of the correlation function  $C(t-t') \equiv \langle x(t)x(t') \rangle$ , or, equivalently,  $\langle \tilde{x}(f)\tilde{x}^*(f') \rangle = \frac{1}{2}P_x(f)\delta(f-f')$ , where  $\tilde{x}(f)$  is the Fourier transform of  $x(t)$ . See also Eq. (3.5).

<sup>3</sup>Our toy-model simulation for BBH ringdown is simply a damped sinusoid with frequency 440 Hz. It has the correct qualitative behavior for a BBH ringdown, but is not meant to be astrophysically realistic.

### 3 Mathematical characterization of a stochastic background

Since the individual signals comprising a GWB background are either too weak or too numerous to individually detect, the combined signal for the background is for all practical purposes *random*, similar to noise in a single detector. Hence, we need to describe the GWB *statistically*, in terms of moments (i.e., ensemble averages) of the metric perturbations describing the GWB.

#### 3.1 Plane-wave expansion

Recall that gravitational waves are time-varying perturbations to the geometry of space-time, which propagate away from the source at the speed of light. In transverse-traceless coordinates  $(t, \vec{x}) \equiv (t, x^a)$ , where  $a = 1, 2, 3$ , the metric perturbations corresponding to a plane wave (propagating in direction  $\hat{k} \equiv -\hat{n}$ ) have two degrees of freedom, corresponding to the amplitudes of the plus (+) and cross ( $\times$ ) polarizations of the gravitational wave (Figure 8). The metric perturbation for the

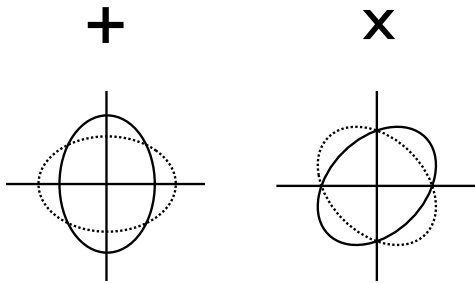


Figure 8: The two orthogonal polarizations of a gravitational wave. A circular ring of test particles in the plane orthogonal to the direction of propagation of the wave are alternately deformed into ellipses, as space is “squeezed” and “stretched” by the passing of the wave.

most general GWB can thus be written as a superposition of such waves:

$$h_{ab}(t, \vec{x}) = \int_{-\infty}^{\infty} df \int d^2\Omega_{\hat{k}} \sum_{A=+, \times} h_A(f, \hat{k}) e_{ab}^A(\hat{k}) e^{i2\pi f(t - \hat{k} \cdot \vec{x}/c)}, \quad (3.1)$$

where  $f$  denotes the frequency of the component waves,  $\hat{k}$  their direction of propagation, and  $A = +, \times$  their polarization. (The direction to a particular GW source is given by  $\hat{n} = -\hat{k}$ .) The quantities  $e_{ab}^A(\hat{k})$  are polarization tensors, given by

$$\begin{aligned} e_{ab}^+(\hat{k}) &= \hat{l}_a \hat{l}_b - \hat{m}_a \hat{m}_b, \\ e_{ab}^\times(\hat{k}) &= \hat{l}_a \hat{m}_b + \hat{m}_a \hat{l}_b, \end{aligned} \quad (3.2)$$

where  $\hat{l}, \hat{m}$  are any two orthogonal unit vectors in the plane orthogonal to  $\hat{k}$ . Typically, for stochastic background analyses, we take  $\hat{l}, \hat{m}$  to be proportional to the standard angular unit vectors tangent to the sphere, so that  $\{\hat{k}, \hat{l}, \hat{m}\}$  is a right-handed system (Figure 9):

$$\begin{aligned} \hat{k} &= -\sin \theta \cos \phi \hat{x} - \sin \theta \sin \phi \hat{y} - \cos \theta \hat{z} = -\hat{r}, \\ \hat{l} &= +\sin \phi \hat{x} - \cos \phi \hat{y} = -\hat{\phi}, \\ \hat{m} &= -\cos \theta \cos \phi \hat{x} - \cos \theta \sin \phi \hat{y} + \sin \theta \hat{z} = -\hat{\theta}. \end{aligned} \quad (3.3)$$

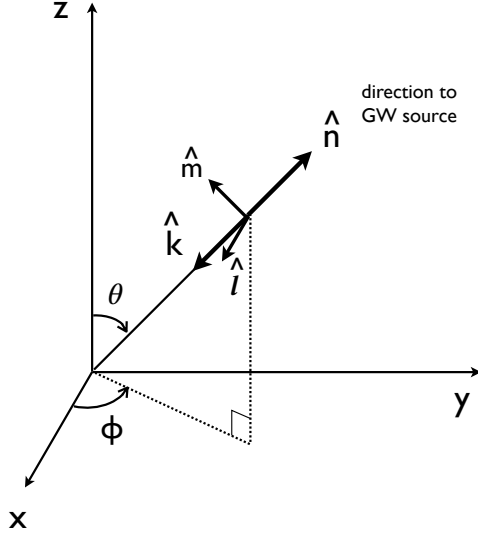


Figure 9: Coordinate system and unit vectors used in the plane-wave expansion of a GWB.

For analyzing non-stochastic GW sources that have a symmetry axis (e.g., the angular momentum vector for binary inspiral), one takes  $\hat{l}$  and  $\hat{m}$  to be rotated relative to  $-\hat{\phi}$  and  $-\hat{\theta}$ , where the rotation angle is the *polarization angle* of the source.

### 3.2 Ensemble averages

The quantities  $h_A(f, \hat{k})$  are the Fourier coefficients of the plane wave expansion. Since the metric perturbations for a stochastic background are random variables, so too are the Fourier coefficients. The probability distributions of the Fourier coefficients thus define the statistical properties of the background.

Without loss of generality, we can assume that the expected value of the Fourier coefficients is zero,

$$\langle h_A(f, \hat{k}) \rangle = 0, \quad (3.4)$$

where angle brackets denote *ensemble average* over different realizations of the background. (The different realizations could be thought of as the different backgrounds observed by different spatially-located observers in a homogeneous and isotropic universe.) The second-order moments (i.e., quadratic expectation values) specify possible correlations between the Fourier coefficients. For example, if the background is *unpolarized, stationary, and isotropic*, then

$$\langle h_A(f, \hat{k}) h_{A'}^*(f', \hat{k}') \rangle = \frac{1}{16\pi} S_h(f) \delta(f - f') \delta_{AA'} \delta^2(\hat{k}, \hat{k}'), \quad (3.5)$$

where  $S_h(f)$  is the *strain power spectral density* of the background, having units of strain<sup>2</sup> Hz<sup>-1</sup>. The fact that the RHS is proportional to  $\delta(f - f')$  is a consequence of the assumption of *stationarity*—i.e., that there is no preferred origin of time. That the RHS depends on the polarization indices only via  $\delta_{AA'}$  is a consequence of the background being unpolarized—i.e., that the + and  $\times$  polarization components are statistically equivalent and uncorrelated with one another. Similarly, the dependence on GW propagation directions only via  $\delta(\hat{k}, \hat{k}')$  is a consequence of exact isotropy, i.e., that the power in the GWB has no preferred direction, and that the GWs propagating in different directions have uncorrelated phases.

If we drop the last assumption, allowing the background to be either *anisotropic* or *statistically isotropic*, then the quadratic expectation values become

$$\langle h_A(f, \hat{k}) h_{A'}^*(f', \hat{k}') \rangle = \frac{1}{4} \mathcal{P}(f, \hat{k}) \delta(f - f') \delta_{AA'} \delta^2(\hat{k}, \hat{k}'), \quad (3.6)$$

where

$$S_h(f) = \int d^2\Omega_{\hat{k}} \mathcal{P}(f, \hat{k}). \quad (3.7)$$

Here  $\mathcal{P}(f, \hat{k})$  is the strain power spectral density per unit solid angle, with units strain<sup>2</sup> Hz<sup>-1</sup> sr<sup>-1</sup>. For statistically isotropic backgrounds, the angular power spectra  $C_l$  are the coefficients of a Legendre series expansion (2.1) of the two-point function  $C(\theta) \equiv \langle \mathcal{P}(f, \hat{k}) \mathcal{P}(f, \hat{k}') \rangle_{\text{sky avg}}$ , for all  $\hat{k}, \hat{k}'$  having  $\cos \theta = \hat{k} \cdot \hat{k}'$ .

For *Gaussian* backgrounds, all cubic and higher-order moments are either identically zero or can be written in terms of the second-order moments. Thus, the quadratic expectation values of the Fourier coefficients completely characterize the statistical properties of a Gaussian-distributed background.

### 3.3 Energy density spectrum in gravitational waves

As mentioned above,  $S_h(f)$  is the strain power spectral density of the GWB. It can be related to the (normalized) *energy density spectrum*

$$\Omega_{\text{gw}}(f) \equiv \frac{1}{\rho_c} \frac{d\rho_{\text{gw}}}{d\ln f} = \frac{f}{\rho_c} \frac{d\rho_{\text{gw}}}{df}, \quad (3.8)$$

where  $d\rho_{\text{gw}}$  is the energy density in gravitational waves contained in the frequency interval  $f$  to  $f + df$ , and  $\rho_c \equiv 3H_0^2 c^2 / 8\pi G$  is the *critical* energy density (that needed to just close the universe today). The result is

$$S_h(f) = \frac{3H_0^2}{2\pi^2} \frac{\Omega_{\text{gw}}(f)}{f^3}, \quad (3.9)$$

which makes use of the relation

$$\rho_{\text{gw}} = \frac{c^2}{32\pi G} \langle \dot{h}_{ab}(t, \vec{x}) \dot{h}^{ab}(t, \vec{x}) \rangle, \quad (3.10)$$

which gives the energy density in gravitational waves in terms of the quadratic expectation values of the metric perturbations. You are asked in Exercise 2 to derive (3.9); to do so, you will also need to use the plane-wave expansion (3.1) and the quadratic expectation values (3.5) or (3.6).

In addition to  $S_h(f)$  and  $\Omega_{\text{gw}}(f)$ , one sometimes describes the strength of a GWB in terms of the (dimensionless) *characteristic strain*  $h_c(f)$  defined by

$$h_c(f) = \sqrt{f S_h(f)}. \quad (3.11)$$

For backgrounds described by a power-law dependence on frequency,<sup>4</sup>

$$h_c(f) = A_\alpha \left( \frac{f}{f_{\text{ref}}} \right)^\alpha \Leftrightarrow \Omega_{\text{gw}}(f) = \Omega_\beta \left( \frac{f}{f_{\text{ref}}} \right)^\beta, \quad (3.12)$$

---

<sup>4</sup>There is no sum over  $\alpha$  or  $\beta$  in the following expressions.

where  $\alpha$  and  $\beta$  are spectral indices, and  $A_\alpha$  and  $\Omega_\beta$  are the amplitudes of the characteristic strain and energy density spectrum, respectively, at some reference frequency  $f = f_{\text{ref}}$ . Using the above definitions and relationships between  $\Omega_{\text{gw}}(f)$ ,  $S_h(f)$ , and  $h_c(f)$ , we have

$$\Omega_\beta = \frac{2\pi^2}{3H_0^2} f_{\text{ref}}^2 A_\alpha^2, \quad \beta = 2\alpha + 2. \quad (3.13)$$

For standard inflationary backgrounds,  $\Omega_{\text{gw}}(f) = \text{const}$ , for which  $\beta = 0$  and  $\alpha = -1$ . For GWBs associated with binary inspiral,  $\Omega_{\text{gw}}(f) \propto f^{2/3}$  (as we shall show below), for which  $\beta = 2/3$  and  $\alpha = -2/3$ . This last dependence is valid for both compact binary coalescences consisting of NSs and/or stellar-mass BHs (relevant for advanced LIGO, Virgo, etc.), and also for inspirals of SMBHs in the centers of distant galaxies (relevant for pulsar timing searches).

### 3.4 Calculating $\Omega_{\text{gw}}(f)$ for an astrophysically-generated background

There is a relatively simple formula for calculating the energy density spectrum  $\Omega_{\text{gw}}(f)$  produced by a collection of discrete astrophysical GW sources distributed throughout the universe[1]:

$$\Omega_{\text{gw}}(f) = \frac{1}{\rho_c} \int_0^\infty dz n(z) \frac{1}{1+z} \left( f_s \frac{dE_{\text{gw}}}{df_s} \right) \Big|_{f_s=f(1+z)}. \quad (3.14)$$

We will call this the “Phinney formula”, since it was first written down by E.S. Phinney in an unpublished paper in 2001. For this expression, one needs only the comoving number density of sources  $n(z)$  as a function of the cosmological redshift  $z$ , and the energy spectrum of an individual source  $dE_{\text{gw}}/df_s$  as measured in its rest frame. The source frame frequency  $f_s$  is related to the observed (present-day) frequency  $f$  via  $f_s = f(1+z)$ . The factor of  $1/(1+z)$  in the integrand is needed to redshift the energy measured in the source frame to that measured today.

The above relationship can also be written in terms of the comoving rate density  $R(z)$ , which is related to the comoving number density  $n(z)$  via

$$n(z) dz = R(z) |dt|_{t=t(z)}. \quad (3.15)$$

The result is

$$\Omega_{\text{gw}}(f) = \frac{f}{\rho_c H_0} \int_0^\infty dz R(z) \frac{1}{(1+z)E(z)} \left( \frac{dE_{\text{gw}}}{df_s} \right) \Big|_{f_s=f(1+z)}, \quad (3.16)$$

where

$$E(z) \equiv \sqrt{\Omega_m(1+z)^3 + \Omega_\Lambda} \quad (3.17)$$

is a cosmological factor that arises when evaluating  $dt/dz$ .  $\Omega_m$  and  $\Omega_\Lambda$  are the fractional energy densities for matter (ordinary baryonic matter plus dark matter) and dark energy, with numerical values roughly equal to 0.30 and 0.70, respectively. Exercise 3 asks you to prove this “rate-version” of the Phinney formula, filling in some of the cosmology-related details.

#### 3.4.1 Example: $\Omega_{\text{gw}}(f)$ for binary inspiral

To illustrate the Phinney formula in action, we will verify the  $\Omega_{\text{gw}}(f) \propto f^{2/3}$  power-law dependence for binary inspiral, which we stated without proof at the end of Section 3.3. Since we are interested here only in the frequency dependence of  $\Omega_{\text{gw}}(f)$ , all we need to calculate is the energy spectrum  $dE_{\text{gw}}/df_s$  for a single binary system.

So let us consider two masses,  $m_1$  and  $m_2$ , in circular orbits around their common center of mass (Figure 10). We make the standard definitions

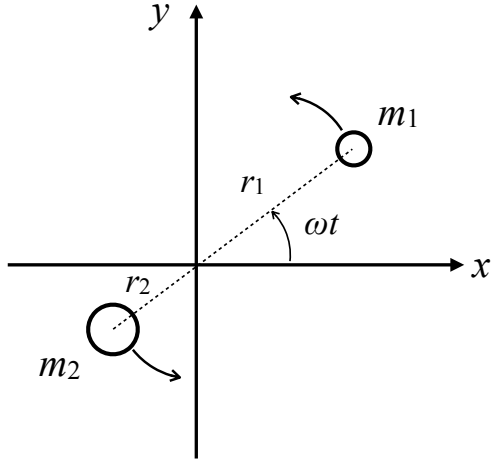


Figure 10: Two masses  $m_1, m_2$  in orbit around their common of mass.

$$r \equiv r_1 + r_2, \quad M \equiv m_1 + m_2, \quad \mu \equiv \frac{m_1 m_2}{m_1 + m_2} \quad (3.18)$$

of the *relative separation*, *total mass*, and *reduced mass* of the system. In terms of these quantities, Kepler's third law and the total orbital energy of the system can be written as

$$\omega^2 r^3 = GM, \quad E_{\text{orb}} = -\frac{GM\mu}{2r}, \quad (3.19)$$

where  $\omega \equiv 2\pi f_{\text{orb}}$  is the orbital angular frequency. The power emitted in gravitational waves comes from the orbital energy

$$\frac{dE_{\text{gw}}}{dt} = -\frac{dE_{\text{orb}}}{dt}, \quad (3.20)$$

which implies that the energy spectrum is given by

$$\frac{dE_{\text{gw}}}{df_s} = \frac{dt}{df_s} \frac{dE_{\text{gw}}}{dt} = -\frac{dt}{df_s} \frac{dE_{\text{orb}}}{dt}. \quad (3.21)$$

It is now a relatively simple matter to evaluate the RHS of the last expression, using Kepler's law to replace all occurrences of  $r$  and  $\dot{r}$  with expressions involving  $\omega$  and  $\dot{\omega}$ . The final result is

$$\frac{dE_{\text{gw}}}{df_s} \sim \mathcal{M}_c^{5/3} f_s^{-1/3}, \quad \mathcal{M}_c^{5/3} \equiv M^{2/3} \mu, \quad (3.22)$$

where  $\mathcal{M}_c$  is the *chirp mass* of the system, and where we have ignored all numerical factors. Note that we also replaced the orbital angular frequency  $\omega$  by the GW frequency  $f_s = 2f_{\text{orb}}$ , with the factor of 2 arising for quadrupolar radiation in general relativity.<sup>5</sup> Returning now to (3.16), we substitute  $f_s = (1+z)f$  and multiply by the factor of  $f$  outside the integral to get  $\Omega_{\text{gw}}(f) \propto f^{2/3}$  as claimed.

---

<sup>5</sup>For elliptical orbits, one should average the radiated power, etc., over a period of the orbit. There will also be contributions to the gravitational radiation from harmonics other than just the quadrupole.

## 4 Correlation methods

As discussed above, a stochastic background of GWs is described by a *random* signal, which looks like noise in a single detector. As such, standard search techniques like *matched filtering*, which correlate the data against known, deterministic waveforms (e.g., BBH chirps) won't work when trying to detect a GWB. Instead, we have to consider other possibilities: (i) One possibility is to know the noise sources in our GW detector well enough (in both amplitude and spectral shape) that we can attribute any unexpected excess "noise" to a GWB. (This was basically how Penzias and Wilson initially detected the CMB; they saw an excess noise temperature of  $\sim 3.5^\circ$  K in their radio antenna that they could not attribute to any other noise source.) (ii) Another possibility is to use data from multiple detectors. Then we can look for evidence of a common disturbance in the multiple data streams consistent with each detector's response to gravitational waves.

Currently, (i) is not an option for ground-based interferometers since, even though the individual noise sources are understood pretty well, their amplitude is not known precisely enough to attribute any observed excess power to gravitational waves. One would need a really loud GWB relative to the detector noise in order detect it in a way similar to Penzias and Wilson's detection of the CMB. But (ii) is an option as LIGO consists of two detectors, one in Hanford, WA, the other in Livingston, LA. Virgo, in Italy, provides a third detector, and soon we will have two more large-scale interferometers in Japan and India. Cross-correlating data from multiple detectors works for detecting a GWB since, even though the signal is random, it is the *same* signal in the different detectors (modulo the physical separation and relative orientation of the detectors). In effect, the random output of one detector is used as a template for the data in another detector. As we shall see below, the signal-to-noise ratio of the cross-correlation grows like the square-root of the observation time. Thus, although the GWB might be weak relative to the noise, it can still be extracted from a cross-correlation measurement if it is observed for a long enough period of time.

### 4.1 Basic idea

To illustrate the basic idea behind cross-correlation, we will consider first the simplest possible scenario—i.e, a single sample of data from two colocated and coaligned detectors:

$$\begin{aligned} d_1 &= h + n_1, \\ d_2 &= h + n_2. \end{aligned} \tag{4.1}$$

Here  $h$  denotes the common GW signal component, and  $n_1, n_2$  denote the corresponding instrumental noise components. Cross-correlating the data for this case amounts to simply taking the product of the two data samples,  $\hat{C}_{12} \equiv d_1 d_2$ . The expected value of the cross-correlation is

$$\langle \hat{C}_{12} \rangle = \langle d_1 d_2 \rangle = \langle h^2 \rangle + \cancel{\langle hn_2 \rangle}^0 + \cancel{\langle n_1 h \rangle}^0 + \langle n_1 n_2 \rangle, \tag{4.2}$$

where  $\langle hn_2 \rangle = 0 = \langle n_1 h \rangle$ , since the GW signal and instrumental noise are not correlated with one another. If we further assume that the noise in the two detectors is *uncorrelated* (which is a good valid assumption if the detectors are widely separated<sup>6</sup>), then  $\langle n_1 n_2 \rangle = 0$ , leaving

$$\langle \hat{C}_{12} \rangle = \langle h^2 \rangle \equiv S_h, \tag{4.3}$$

which is just the variance (i.e., power) in the GW signal.

---

<sup>6</sup>Note that global magnetic fields, e.g., Schumann resonances, *can* produce environmental correlations in widely separated detectors.

## 4.2 Extension to multiple data samples

The above analysis can be easily extended to the case of multiple samples:

$$\begin{aligned} d_{1i} &= h_i + n_{1i}, \\ d_{2i} &= h_i + n_{2i}, \end{aligned} \quad (4.4)$$

where  $i = 1, 2, \dots, N$ . As before, we will assume that the two detectors are coincident and coaligned, and that the noise in the two detectors are uncorrelated with the GW signal and with one another

$$\langle n_{1i}h_j \rangle = 0, \quad \langle n_{2i}h_j \rangle = 0, \quad \langle n_{1i}n_{2j} \rangle = 0. \quad (4.5)$$

We will also assume that the GWB and detector noise are both *white*, which means

$$\langle h_ih_j \rangle = S_h \delta_{ij}, \quad \langle n_{1i}n_{1j} \rangle = S_{n1} \delta_{ij}, \quad \langle n_{2i}n_{2j} \rangle = S_{n2} \delta_{ij}, \quad (4.6)$$

where  $S_h, S_{n1}, S_{n2}$  are the variances (i.e., power) in the GW signal and detector noise, respectively.<sup>7</sup> For this case, our cross-correlation statistic is the average of the products of the individual data samples

$$\hat{S}_h \equiv \hat{C}_{12} \equiv \frac{1}{N} \sum_{i=1}^N d_{1i}d_{2i}, \quad (4.7)$$

which, as we shall see below, is again an estimator of the power in the GWB (hence the “hat” ( $\hat{\cdot}$ ) over the  $S_h$  on the LHS of this equation).

Using the above definitions and quadratic expectation values, it is easy to show that

$$\mu \equiv \langle \hat{C}_{12} \rangle = \frac{1}{N} \sum_{i=1}^N \langle d_{1i}d_{2i} \rangle = \frac{1}{N} \sum_{i=1}^N \langle h_i^2 \rangle = S_h. \quad (4.8)$$

Thus, the cross-correlation statistic  $\hat{C}_{12}$  is an (unbiased) estimator of the GW power  $S_h$ . The variance in this estimator can be calculated via

$$\sigma^2 \equiv \langle \hat{C}_{12}^2 \rangle - \langle \hat{C}_{12} \rangle^2 = \left( \frac{1}{N} \right)^2 \sum_{i=1}^N \sum_{j=1}^N (\langle d_{1i}d_{2i}d_{1j}d_{2j} \rangle - \langle d_{1i}d_{2i} \rangle \langle d_{1j}d_{2j} \rangle). \quad (4.9)$$

To evaluate the RHS of the above equation, we make use of the identity

$$\langle abcd \rangle = \langle ab \rangle \langle cd \rangle + \langle ac \rangle \langle bd \rangle + \langle ad \rangle \langle bc \rangle, \quad (4.10)$$

which is valid for zero-mean Gaussian random variables. Using this identity and the quadratic expectation values between the signal and noise, we end up with

$$\sigma^2 = \frac{1}{N} (S_1 S_2 + S_h^2), \quad (4.11)$$

where

$$S_1 \equiv S_{n1} + S_h, \quad S_2 \equiv S_{n2} + S_h, \quad (4.12)$$

---

<sup>7</sup>The assumption that both the GWB and detector noise are white is made here just to simplify the analysis. One can use cross-correlation methods for the more general case where the signal and noise power spectral densities are non-trivial functions of frequency [?].

are the total power in the detector output (consisting of both signal and noise power). Note that the factor of  $1/N$  in (4.11) comes from the double sum in (4.9) having non-zero contributions from only the diagonal terms ( $i = j$ ), which are all equal to one another.

Since the power in the GWB is expected to be weak compared to the detector noise, the variance can be approximated as  $\sigma^2 \simeq S_1 S_2 / N$ , for which the expected signal-to-noise ratio is given by

$$\rho \equiv \frac{\mu}{\sigma} \simeq \frac{S_h}{\sqrt{S_1 S_2 / N}} \simeq \sqrt{N} \frac{S_h}{S_n}, \quad (4.13)$$

where  $\sqrt{S_1 S_2} \simeq \sqrt{S_{n1} S_{n2}} \equiv S_n$ . This result verifies the statement made earlier that the signal-to-noise ratio for a cross-correlation measurement grows like the square-root of the observation time (in this case, the total number of samples).

### 4.3 Optimal filtering

To handle the case of physically-separated and misaligned detectors, we need to include the non-trivial response of a GW detector to a GWB. We will do this in more detail in Sections 6 and 7. Here, it suffices to simply define the *overlap function* (or overlap reduction function), denoted  $\Gamma_{12}(f)$ , as the transfer function relating the strain power in the GWB,  $S_h(f)$ , to the cross-correlated signal power in the two detectors,

$$C_{12}(f) \equiv \Gamma_{12}(f) S_h(f). \quad (4.14)$$

(We will derive the form of  $\Gamma_{12}(f)$  and discuss more of its properties in Section 7.) In terms of the quadratic expectation values of the GW signal in the two detectors, we have<sup>8</sup>:

$$\langle \tilde{h}_1(f) \tilde{h}_2^*(f') \rangle = \frac{1}{2} \delta(f - f') \Gamma_{12}(f) S_h(f), \quad (4.15)$$

where  $\tilde{h}_1(f)$ ,  $\tilde{h}_2(f)$  denote the Fourier transforms of GW signal components  $h_1(t)$ ,  $h_2(t)$  in the two detectors. For comparison, the (auto-correlated) power spectra of the detector noise  $P_{n1}(f)$ ,  $P_{n2}(f)$  can be written in terms of the noise components  $\tilde{n}_1(f)$ ,  $\tilde{n}_2(f)$  via:

$$\begin{aligned} \langle \tilde{n}_1(f) \tilde{n}_1^*(f') \rangle &= \frac{1}{2} \delta(f - f') P_{n1}(f), \\ \langle \tilde{n}_2(f) \tilde{n}_2^*(f') \rangle &= \frac{1}{2} \delta(f - f') P_{n2}(f), \end{aligned} \quad (4.16)$$

while the cross-correlated noise is assumed to be zero:

$$\langle \tilde{n}_1(f) \tilde{n}_2^*(f') \rangle = 0. \quad (4.17)$$

Plots of  $\Gamma_{12}(f)$  for the LIGO Hanford-LIGO Livingston interferometer pair and for the LIGO Hanford-Virgo interferometer pair can be found in Section 7.

Given the above definitions, we can now ask the question: “What is the optimal way to correlate data from two physically separated and possibly mis-aligned detectors to search for a GWB?” To answer this question, we start by forming the generic cross-correlation

$$\hat{C}_{12} = \int_{-T/2}^{T/2} dt \int_{-T/2}^{T/2} dt' d_1(t) d_2(t) Q(t, t'), \quad (4.18)$$

---

<sup>8</sup>The factor of  $1/2$  is included on the RHS so that the power spectrum is *one-sided*. In other words, the total cross-correlated power in the GWB is given by the integral of  $\Gamma_{12}(f) S_h(f)$  over just the *positive* frequencies. The factor of  $\delta(f - f')$  is a consequence of stationarity.

where  $Q(t, t')$  is an a priori arbitrary filter function and  $T$  is the observation time. For stationary data,  $Q(t, t')$  should depend only on the difference between the two time arguments,  $\Delta t \equiv t - t'$ , so that  $Q(t, t') \equiv Q(t - t')$ . In the Fourier domain, we can then write

$$\hat{C}_{12} \simeq \int_{-\infty}^{\infty} df \int_{-\infty}^{\infty} df' \delta_T(f, f') \tilde{d}_1(f) \tilde{d}_2(f') \tilde{Q}^*(f'), \quad (4.19)$$

where  $\tilde{Q}(f)$  is the Fourier transform of  $Q(\Delta t)$ , and  $\delta_T(f - f')$  is a finite-time version of the Dirac delta function defined by  $\delta_T(f - f') \equiv T \text{sinc}(\pi(f - f'))$ , where  $\text{sinc } x \equiv \sin x / x$ .

To proceed further we need to define what we mean by *optimal*. A natural criterion in this context is to maximize the expected signal-to-noise ratio of  $\hat{C}_{12}$  for a GWB with a fixed spectral shape  $H(f)$ . (The expected signal-to-noise ratio is defined as in the previous section  $\rho \equiv \mu/\sigma$ , where  $\mu \equiv \langle \hat{C}_{12} \rangle$  and  $\sigma^2 \equiv \langle \hat{C}_{12}^2 \rangle - \langle \hat{C}_{12} \rangle^2$ .) As you are asked to show in Exercise 4, this maximization condition determines the form of the filter function  $\tilde{Q}(f)$  up to an overall normalization:

$$\tilde{Q}(f) \propto \frac{\Gamma_{12}(f) H(f)}{P_1(f) P_2(f)}, \quad (4.20)$$

where  $P_1(f)$ ,  $P_2(f)$  are the total power in the two detectors,

$$P_1(f) \equiv P_{n1}(f) + P_h(f), \quad P_2(f) \equiv P_{n2}(f) + P_h(f), \quad (4.21)$$

which are approximately equal to  $P_{n1}(f)$ ,  $P_{n2}(f)$  under the assumption that the GW signal is weak compared to the detector noise. Note that the numerator of  $\tilde{Q}(f)$  is proportional to the expected value of the cross-correlated data in the frequency domain,  $\langle \tilde{d}_1(f) \tilde{d}_2^*(f) \rangle$ , while the denominator basically de-weights the correlation when the detector noise is large. The dependence of  $\tilde{Q}(f)$  on the spectral shape  $H(f)$  means that the optimal filter is tuned to a particular GWB.

The overall normalization of the optimal filter  $\tilde{Q}(f)$  is not determined by the maximization condition, since a constant multiplicative factor cancels out when calculating the signal-to-noise ratio  $\rho = \mu/\sigma$ . Typically, we use this freedom in the choice of normalization to set the expected value  $\mu$  of the cross-correlation equal to the overall amplitude of the background—i.e.,  $\mu = \Omega_{\text{gw}}(f_{\text{ref}})$ . In other words, for this choice of normalization, the measured value of the cross-correlation statistic,  $\hat{C}_{12}$ , is a *point estimate* of  $\Omega_{\text{gw}}(f_{\text{ref}})$ .

## 5 Optimal filtering applied to some simple examples

We now apply the above correlation methods to analyze some simple examples involving simulated data. (The simulations are solely meant to illustrate how optimal filtering works; the amplitude and duration of the simulated data are not representative of real interferometer data.<sup>9</sup>) We will consider three different GWBs injected into uncorrelated, white detector noise in two coincident and coaligned detectors: (i) a white GWB, (ii) a confusion-limited BNS background, and (iii) a two-component background, formed from the superposition of the GWBs from (i) and (ii). The simulated time-domain data for the three different cases are shown in Figure 11. Recall that a white GWB has a flat spectrum  $H(f) = 1$ , while a confusion-limited background produced by BNS inspirals and mergers has spectral shape  $H(f) = (f/f_{\text{ref}})^{-7/3}$  (see Figure 7).

---

<sup>9</sup>The simulated data used for these examples can be found at [?]. Access to real GW data is available via the Gravitational-Wave Open Science Center (GWOSC) [?].

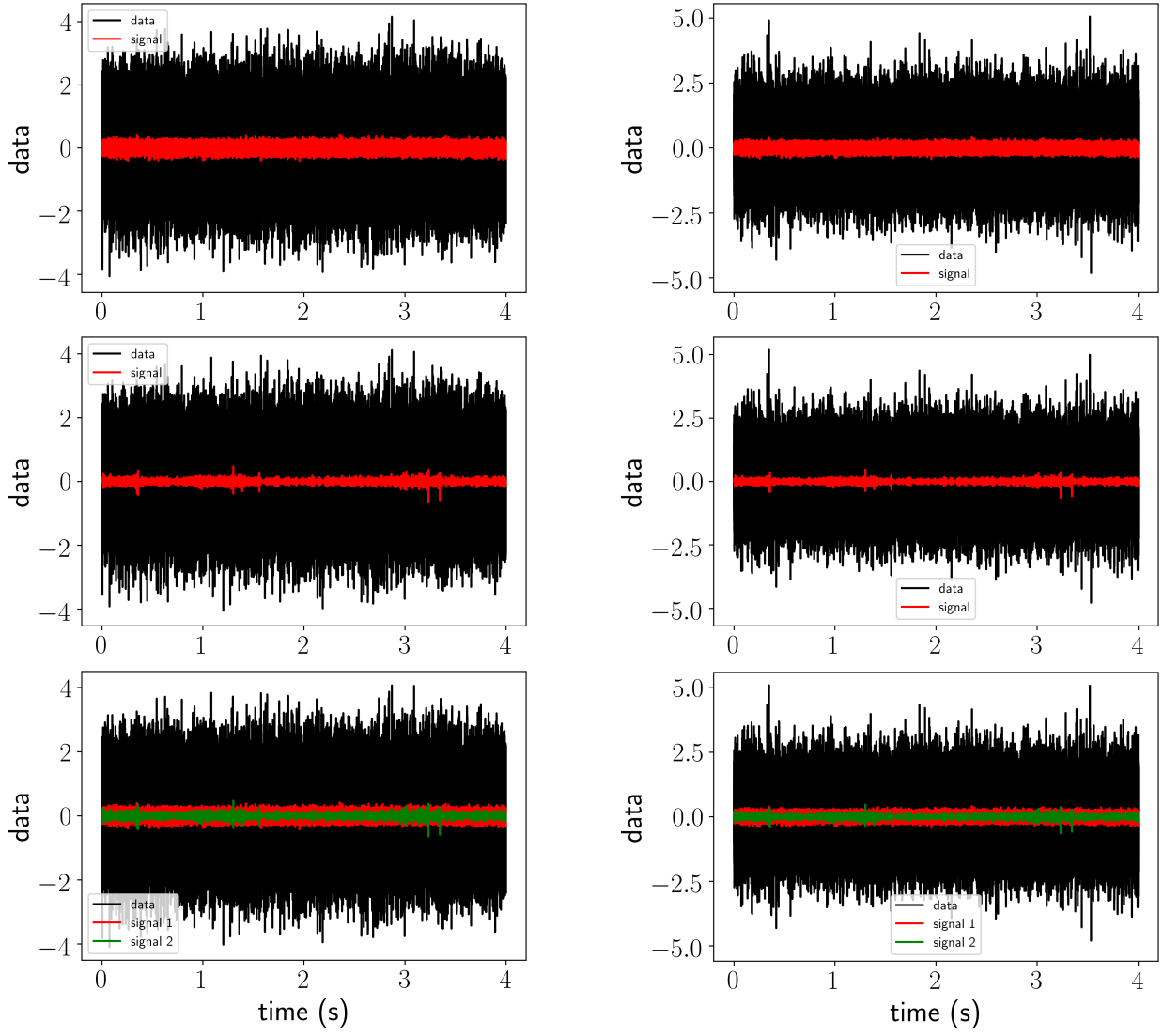


Figure 11: Simulated time-domain data for the three different cases discussed in the main text: (top row) a white GWB in uncorrelated, white detector noise, (middle row) a confusion-limited BNS background in uncorrelated, white detector noise, (bottom row) a two-component background formed from the superposition of the GWBs from the top two rows in uncorrelated, white detector noise. The two columns correspond to data in the two coincident and coaligned detectors. By eye one can see that signal components in the two detectors are identical, but the noise (and hence the data) in the two detectors are different.

## 5.1 Single-component analyses

We start by applying the single-component optimal-filter analysis of the previous section. For example (i), we find that the measured and injected values of the amplitude of the GWB agree to 3.5%, which is within  $1-\sigma$ . The corresponding optimally-filtered signal-to-noise ratio is  $\rho = 2.9$ . For example (ii), the measured and injected values of the amplitude of the GWB agree to 2.7%, which again is within  $1-\sigma$ . The corresponding optimally-filtered signal-to-noise ratio for this case is  $\rho = 12$ . Note that even though the overall amplitude of the background is noticeably smaller for the confusion-limited BNS background, the signal-to-noise ratio is considerably larger (12 versus 2.9). This is because the spectrum of the GW signal differs in this case from that of the detector noise, which helps in distinguishing the signal and noise components.

Finally for example (iii), if we filter the data for the two components separately, we overestimate the amplitude of the white GWB component by 48%, which is greater than  $1-\sigma$ , and overestimate the amplitude of the BNS background by 6.9%, which is within  $1-\sigma$ . Basically, filtering the data for each GWB component separately typically leads to *overestimates* of the amplitudes of the individual components, but *underestimates* of the error bars. The overestimates arise since the other GWB component is also contributing to the correlated signal.

## 5.2 Multi-component analysis

To better extract the amplitudes of the individual components for example (iii), we need to go beyond single-component optimal-filtering, and consider a signal model that allows for a superposition of multiple GWB components [?]. So instead of taking the cross-correlation to be a *single number*,  $\hat{C}_{12}$ , which is obtained by integrating the contributions from all frequencies, we will keep the frequency-dependence explicit, defining

$$\hat{C}_{12}(f) \equiv \frac{2}{T} \tilde{d}_1(f) \tilde{d}_2^*(f), \quad (5.1)$$

where  $\tilde{d}_1(f)$ ,  $\tilde{d}_2(f)$  are the Fourier transforms of the time-domain data  $d_1(t)$ ,  $d_2(t)$  from the two detectors. We will treat the values of  $\hat{C}_{12}(f)$  for different frequencies  $f$  as the ‘data points’ from which to construct a *likelihood function*, which is the probability of the data given the parameters defining the signal and noise models.<sup>10</sup> For this case, the signal model is given by the expected value of the correlated data:

$$\langle \hat{C}_{12}(f) \rangle = \sum_{\alpha} \Gamma_{12}(f) A_{\alpha} H_{\alpha}(f) \equiv \sum_{\alpha} M_{\alpha}(f) A_{\alpha}, \quad (5.2)$$

where  $H_{\alpha}(f)$  are the different spectral shapes having amplitudes  $A_{\alpha}$ . (Abstractly, we can think of  $M_{\alpha}(f) \equiv \Gamma_{12}(f) H_{\alpha}(f)$  as a matrix with indices  $f$  and  $\alpha$ , where  $f$  runs over different frequency bins and  $\alpha$  runs over different spectral components.) The noise model enters via the covariance matrix of the data:

$$N_{12}(f, f') \equiv \langle \hat{C}_{12}(f) \hat{C}_{12}^*(f') \rangle - \langle \hat{C}_{12}(f) \rangle \langle \hat{C}_{12}^*(f') \rangle \simeq \delta_{ff'} P_1(f) P_2(f), \quad (5.3)$$

---

<sup>10</sup>See John Veitch’s lectures in this Volume for more details regarding likelihood functions and Bayesian inference.

which is the product of the noise power spectra in the two detectors in the weak-signal approximation. The likelihood function is then<sup>11</sup>

$$p(\hat{C}|A, N) \propto \exp \left[ -\frac{1}{2}(\hat{C} - MA)^\dagger N^{-1}(\hat{C} - MA) \right], \quad (5.4)$$

which is the probability of the cross-correlated data  $\hat{C}_{12}(f)$  given the amplitudes  $A_\alpha$  of the GWB spectral components and the noise in the two detectors  $N_{12}(f, f')$ .

We can now obtain estimators of the amplitudes of the GWB components, by maximizing the likelihood function with respect to the  $A_\alpha$ . The final result (which you are asked to show in Exercise 5) is:

$$\hat{A} = F^{-1}X, \quad (5.5)$$

where

$$F \equiv M^\dagger N^{-1} M, \quad X \equiv M^\dagger N^{-1} \hat{C}. \quad (5.6)$$

The quantity  $F$  is called the *Fisher information matrix*. In terms of its components,

$$F_{\alpha\beta} = \int_{-\infty}^{\infty} df \frac{H_\alpha(f)\Gamma_{12}^2(f)H_\beta(f)}{P_1(f)P_2(f)}. \quad (5.7)$$

Thus, we see that the Fisher matrix is a noise-weighted inner product of the spectral shapes  $H_\alpha(f)$ ,  $H_\beta(f)$  with one another. Provided the spectral shapes are not degenerate (i.e., not proportional to one another), then the Fisher matrix  $F$  can be inverted and  $\hat{A}$  calculated. Otherwise, some form of regularization is needed to perform the matrix inversion. The inverse of the Fisher matrix,  $F^{-1}$ , turns out to equal the covariance matrix of the estimators  $\hat{A}$ .

Using the above multi-component formalism, we are now able to extract the amplitude of the white GWB component to 7.3%, corresponding to a signal-to-noise ratio of 1.4, and to extract the amplitude of the BNS background component to 3.8%, corresponding to a signal-to-noise ratio of 6.0. In essence, the *joint* multi-component analysis properly takes into account the *covariance* between the spectral shapes of the two components, allowing for unbiased, minimal variance estimates of the amplitudes  $A_\alpha$ .

## Part II

# Details / Examples

In the second part of these notes, we describe the non-trivial response of a beam detector to gravitational waves, calculate the overlap function between a pair of detectors, and introduce a Bayesian method that can optimally search for the astrophysical background produced by stellar-mass binary BHs and NSs throughout the universe.

---

<sup>11</sup>We are using here an *index-free* matrix notation, dropping the  $\alpha$ ,  $\beta$ ,  $f$ , and  $f'$  indices, as well as the sums and integrals over  $\alpha$  and  $f$ . If we explicitly insert all of the indices, sums, etc., the argument of the exponential becomes

$$-\frac{1}{2} \int_{-\infty}^{\infty} df \frac{|\hat{C}_{12}(f) - \sum_\alpha M_\alpha(f)A_\alpha|^2}{P_1(f)P_2(f)}.$$

## 6 Non-trivial detector response

To understand stochastic background searches on a more quantitative level, we need to describe the non-trivial response of a GW detector to a passing GW. In Section 4.3, we defined the overlap function  $\Gamma_{12}(f)$  for a pair of detectors, but we didn't specify how to calculate it, or how its form differs for different GW detectors. In this and the following section, we will develop the tools that we need to do these calculations.

### 6.1 Beam detectors and different types of detector response

For simplicity, we will restrict our attention to *beam detectors*, which use electromagnetic radiation to monitor the separation of two or more test masses. Laser interferometers (both ground-based and space-based), spacecraft Doppler tracking, and pulsar timing arrays are all examples of beam detectors. (A resonant-bar detector, like that first used by Joseph Weber, is a much different type of detector. Roughly speaking, a resonant bar detector responds like a giant tuning fork to a passing GW, provided the GW has frequencies equal to the resonant frequency of the bar.) The response of a beam detector to a passing GW is the change in the light-travel time between the two masses relative to the nominal light-travel time. This is illustrated schematically in Figure 12.

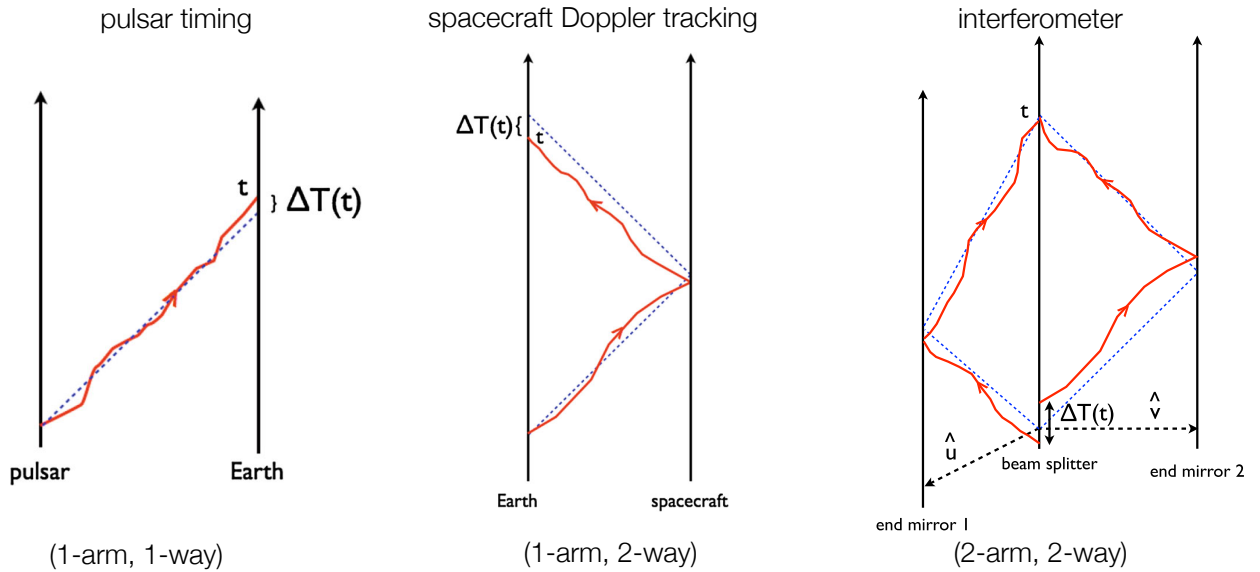


Figure 12: Spacetime diagram showing the response of beam detectors to a passing GW. Left column: pulsar timing; middle column: spacecraft Doppler tracking; right column: interferometer (ground or space-based). A passing GW perturbs the path of the photon (red trajectory) relative to its nominal path in the absence of the wave (blue dotted line), leading to a difference in the expected arrival time of the photon. (Figure adapted from [2].)

In the literature, one might see the detector response written in terms of strain  $\Delta L(t)/L$ , fractional Doppler frequency  $\Delta v(t)/\nu_0$ , or phase  $\Delta\Phi(t)$ , instead of the timing residual  $\Delta T(t)$ . Despite the apparent differences in the responses, they are all derivable from the change in light

travel time  $\Delta T(t)$  via the relations:

$$\begin{aligned}
h(t) &\equiv \Delta T(t) && \text{(pulsar timing)} \\
h(t) &\equiv \frac{\Delta L(t)}{L} = \frac{\Delta T(t)}{T} && \text{(LIGO, Virgo, \dots)} \\
h(t) &\equiv \frac{\Delta\nu(t)}{\nu_0} = \frac{d\Delta T(t)}{dt} && \text{(spacecraft Doppler tracking)} \\
h(t) &\equiv \Delta\Phi(t) = 2\pi\nu_0 \Delta T(t) && \text{(LISA).}
\end{aligned} \tag{6.1}$$

Hence, once we know how to calculate the timing residual response  $\Delta T(t)$ , we can easily calculate all the other quantities listed above.

## 6.2 Detector response functions

GWs are weak. As such, a detector act like a *linear* system, which converts metric perturbations to detector output. Mathematically, this is represented by the *convolution* of the metric perturbations with the *response function* of the detector:

$$h(t) = (\mathbf{R} * \mathbf{h})(t, \vec{x}) \equiv \int_{-\infty}^{\infty} d\tau \int d^3y R^{ab}(\tau, \vec{y}) h_{ab}(t - \tau, \vec{x} - \vec{y}) \tag{6.2}$$

Here  $h(t)$  is the output of the detector at time  $t$ . The vector  $\vec{x}$  is the location of detector, and  $R^{ab}(\tau, \vec{y})$  is the *impulse response* of the detector. Expanding  $h_{ab}(t - \tau, \vec{x} - \vec{y})$  as a sum of plane waves (3.1), we find that the Fourier transform  $\tilde{h}(f)$  of  $h(t)$  can be written as

$$\tilde{h}(f) = \int d^2\Omega_{\hat{n}} \sum_A R^A(f, \hat{n}) h_A(f, \hat{n}) \tag{6.3}$$

where

$$R^A(f, \hat{n}) \equiv R^{ab}(f, \hat{n}) e_{ab}^A(\hat{n}) \tag{6.4}$$

and

$$R^{ab}(f, \hat{n}) \equiv e^{i2\pi f \hat{n} \cdot \vec{x}/c} \int_{-\infty}^{\infty} d\tau \int d^3y R^{ab}(\tau, \vec{y}) e^{-i2\pi f(\tau + \hat{n} \cdot \vec{y}/c)} \tag{6.5}$$

Note that  $R^A(f, \hat{n})$  is the detector response for a plane-wave with frequency  $f$ , propagation direction  $\hat{k}$ , and polarization  $A$ .

## 6.3 Examples

### 6.3.1 Detector response for a one-arm, one-way detector

For our first example, we will consider the timing response of a one-arm, one-way beam detector, which is relevant for pulsar timing observations. The geometry of the situation is shown in Figure 13.

$$h(t) \equiv \Delta T(t) = \frac{1}{2c} u^a u^b \int_0^L ds h_{ab}(t(s), \vec{x}(s)) \tag{6.6}$$

$$t(s) = (t - L/c) + s/c, \quad \vec{x}(s) = \vec{r}_1 + s\hat{u} \tag{6.7}$$

In Exercise 6, you are asked to show that the timing residual response is given by

$$R^A(f, \hat{n}) = \frac{1}{i2\pi f} \frac{1}{2} u^a u^b e_{ab}^A(\hat{n}) \frac{1}{1 + \hat{n} \cdot \hat{u}} \left[ 1 - e^{-\frac{i2\pi f L}{c}(1 + \hat{n} \cdot \hat{u})} \right] e^{i2\pi f \hat{n} \cdot \vec{r}_2/c} \tag{6.8}$$

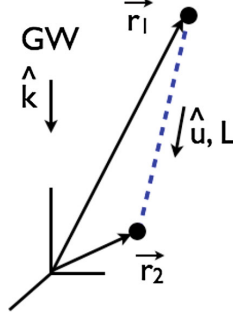


Figure 13: Geometry for a one-arm, one-way beam detector, relevant for a pulsar timing residual measurement. The GW propagates in the  $\hat{k}$  direction; the electromagnetic wave (e.g., a radio pulse from a pulsar) propagates in the  $\hat{u}$  direction (opposite of the direction to the pulsar,  $\hat{p} = -\hat{u}$ ).

In the context of pulsar timing, the two terms in square brackets are called the *Earth term* and *pulsar term* respectively. The pulsar term encodes information about the phase of the GW at the location of the pulsar. It is usually ignored for stochastic background searches, as this term for different pulsars will not be correlated with one other (since the spatial distance between two pulsars is much greater than the wavelengths of the GWs that pulsar timing arrays are sensitive to).

Note that the factor  $1/(i2\pi f)$  goes away for the Doppler frequency response,  $\Delta\nu(t)/\nu_0$ , and that the phase term  $e^{-i2\pi f \hat{k} \cdot \vec{r}_2/c}$  equals one if we take the  $\vec{r}_2$  to be the origin of coordinates, e.g., at the solar system barycentre. Then the Doppler frequency response simplifies to

$$F^A(\hat{k}) = \frac{1}{2} u^a u^b e_{ab}^A(\hat{k}) \frac{1}{1 - \hat{k} \cdot \hat{u}} \quad (6.9)$$

where the last expression is written in terms of the direction to the pulsar  $\hat{p} = -\hat{u}$ . A plot of this response, summed over the two polarizations, is shown in Figure 14. The response is maximum

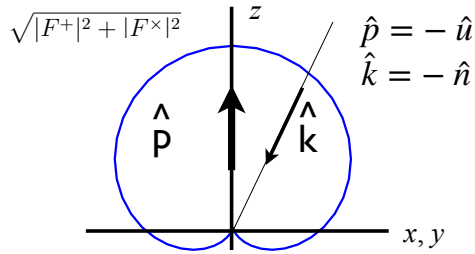


Figure 14: Polarization-averaged Doppler frequency response  $\sqrt{|F^+(\hat{k})|^2 + |F_x(\hat{k})|^2}$  for pulsar timing, ignoring the frequency-dependent part of the pulsar term. The response is axially symmetric around the  $z$ -axis, which we've chose to be the direction to the pulsar  $\hat{p} = -\hat{u}$ .

when the GW and radio pulse propagate in the same direction—i.e., when  $\hat{k} = \hat{u}$ . It is zero when

they propagate in opposite directions. These results follow from

$$\begin{aligned} u^a u^b e_{ab}^+(\hat{k}) &= \sin^2 \theta = (1 - \cos \theta)(1 + \cos \theta), \\ u^a u^b e_{ab}^\times(\hat{k}) &= 0, \end{aligned} \quad (6.10)$$

and

$$\frac{1}{1 - \hat{k} \cdot \hat{u}} = \frac{1}{1 - \cos \theta}, \quad (6.11)$$

where  $\hat{u} = -\hat{z}$  and  $\theta$  is the usual polar angle between  $\hat{k}$  and the  $z$  direction.

### 6.3.2 Detector response for a laser interferometer in the short-antenna limit

Another simple example of a detector response function is for a equal-arm laser interferometer, like LIGO, in the *short-antenna limit* (Figure 15). This approximation is valid when the wavelength

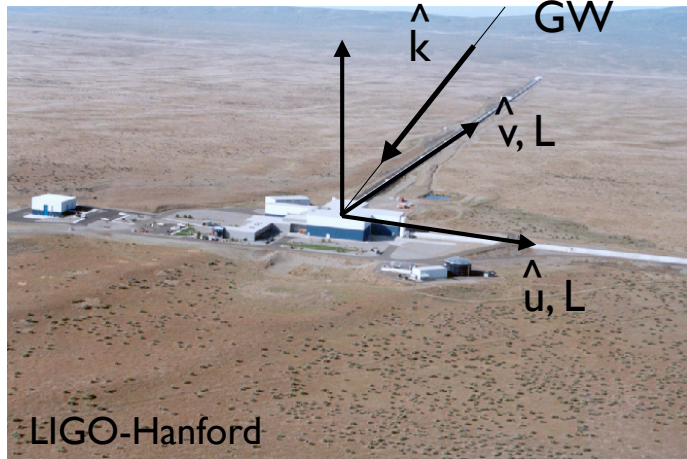


Figure 15: Geometry for a ground-based interferometer GW response calculation. (Shown here the LIGO Hanford Observatory, in Hanford, WA.) The GW propagates in the  $\hat{k}$  direction;  $\hat{u}, \hat{v}$  are unit vectors that point along the two arms of the interferometer. In the short-antenna approximation, the length  $L$  of the arms does not enter the expression for the response function.

of the GW is much larger than the dimensions of the detector. Then, the GW phase is effectively constant as a photon travels down an back an interferometer arm. Defining the strain response of the interferometer as

$$h(t) = \frac{1}{2} \left( \frac{\Delta T_{\vec{u}, \text{roundtrip}}(t)}{T} - \frac{\Delta T_{\vec{v}, \text{roundtrip}}(t)}{T} \right) \quad (6.12)$$

one can show that

$$R^A(f, \hat{n}) \simeq \frac{1}{2} \left( u^a u^b - v^a v^b \right) e_{ab}^A(\hat{n}) \quad (6.13)$$

The quantity multiply  $e_{ab}^A(\hat{k})$  in the reponse function is called the *detector tensor*

$$D^{ab} \equiv \frac{1}{2} \left( u^a u^b - v^a v^b \right). \quad (6.14)$$

Plots of the *beam pattern functions*  $|R^+(f, \hat{k})|$ ,  $|R^\times(f, \hat{k})|$  for the two polarizations individually, and the root-summed-squared response for both polarization  $\sqrt{|R^+(f, \hat{k})|^2 + |R^\times(f, \hat{k})|^2}$  is shown in Figure 16.

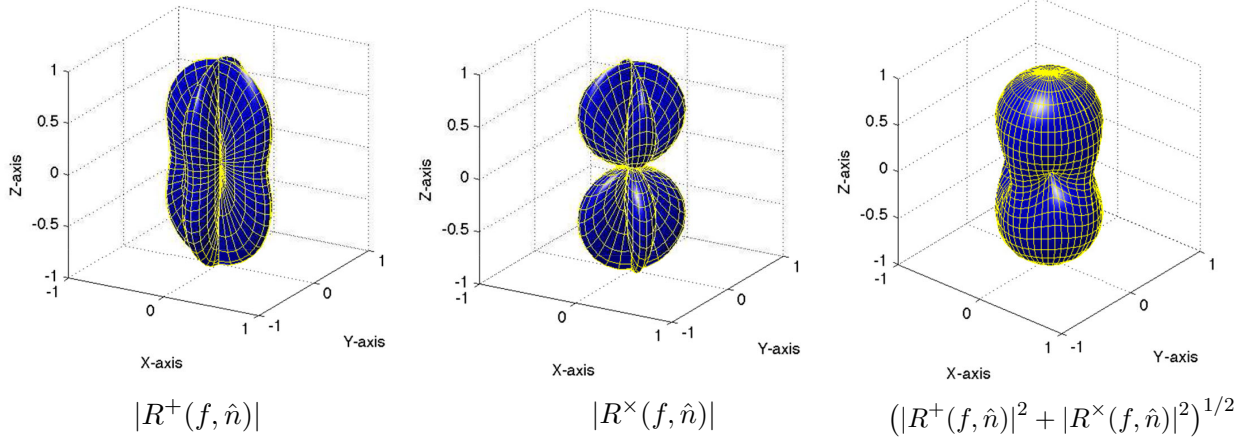


Figure 16: Beam pattern functions for a ground-based interferometer like LIGO in the short-antenna approximation—i.e.,  $f \lesssim$  few kHz. The vertex of the interferometer is at the origin of coordinates, and interferometer arms are assumed to be orthogonal pointing along the  $x$  and  $y$  directions.

## 7 Non-trivial correlations

### 7.1 Overlap function

Detectors in different locations and with different orientations respond differently to a passing GW. Overlap function encodes reduction in sensitivity of a cross-correlation analysis due to separation and misalignment of the detectors.

In the time domain:

$$\langle h_I(t)h_J(t') \rangle = \frac{1}{2} \int_{-\infty}^{\infty} df e^{i2\pi f(t-t')} \Gamma_{IJ}(f) S_h(f) \quad (7.1)$$

In the frequency domain:

$$\langle \tilde{h}_I(f)\tilde{h}_J^*(f') \rangle = \frac{1}{2} \delta(f-f') \Gamma_{IJ}(f) S_h(f) \quad (7.2)$$

One finds

$$\Gamma_{IJ}(f) = \frac{1}{8\pi} \int d^2\Omega_{\hat{n}} \sum_A R_I^A(f, \hat{n}) R_J^{A*}(f, \hat{n}) \quad (7.3)$$

for an unpolarized, stationary isotropic GWB. As mentioned in Section 4.3,  $\Gamma_{IJ}(f)$  is the transfer function between the strain power in the GWB and detector cross-power. The integrand of  $\Gamma_{IJ}(f)$  is important for statistically *anisotropic* backgrounds as the right-hand-side of (7.6) is replaced by

$$\frac{1}{8\pi} \int d^2\Omega_{\hat{k}} \sum_A R_I^A(f, \hat{k}) R_J^{A*}(f, \hat{k}) \mathcal{P}(f, \hat{k}) \quad (7.4)$$

One then typically expands  $\mathcal{P}(f, \hat{k})$  in terms of spherical harmonics

$$\mathcal{P}(f, \hat{k}) = \sum_{l=0}^{\infty} \sum_{m=-l}^l \mathcal{P}_{lm}(f) Y_{lm}(\hat{k}), \quad (7.5)$$

for which (7.6) becomes

$$\langle \tilde{h}_I(f) \tilde{h}_J^*(f') \rangle = \frac{1}{2} \delta(f - f') \sum_{l=0}^{\infty} \sum_{m=-l}^l \Gamma_{IJ,lm}(f, \hat{k}) \mathcal{P}_{lm}(f). \quad (7.6)$$

with

$$\Gamma_{IJ,lm}(f, \hat{k}) = \frac{1}{8\pi} \sum_A R_I^A(f, \hat{k}) R_J^{A*}(f, \hat{k}) Y_{lm}(\hat{k}). \quad (7.7)$$

Interested readers can find much more discussion about anisotropic background in Section 7 of [2], and references to the original work cited therein.

## 7.2 Examples

### 7.2.1 Overlap function for a pair of laser interferometers in the short-antenna limit

Note that the first zero crossing occurs at roughly 60 Hz, corresponding to GW with wavelength equal to twice the separation between the two observatories.

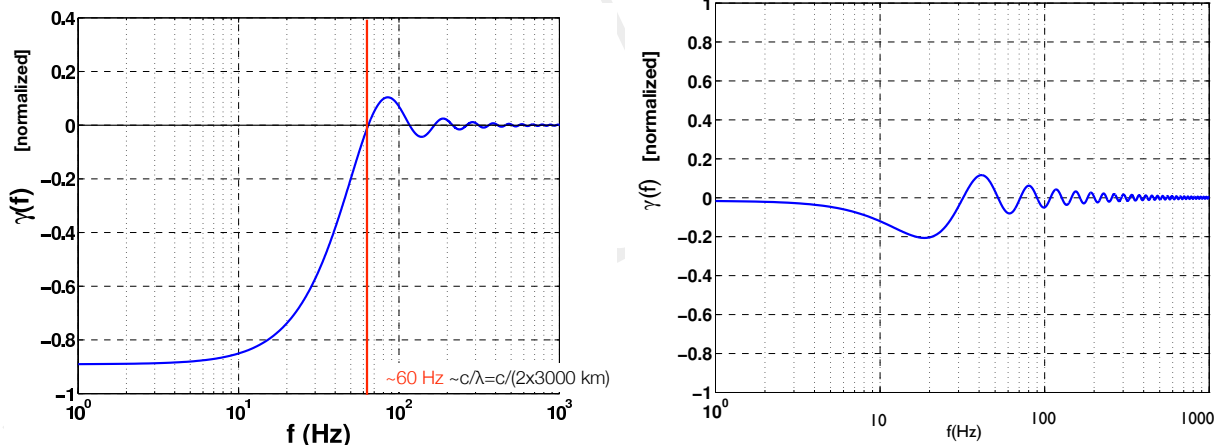


Figure 17: Normalized overlap function for ground-based interferometers. Left panel: LIGO Hanford-LIGO Livingston detector pair. Right panel: LIGO Hanford-Virgo detector pair. These overlap functions were calculated in the small-antenna approximation. Note the reduced amplitude of the LHO-Virgo overlap function relative to the LHO-LLO overlap function due to the much larger separation between Hanford, WA and Pisa, Italy.

### 7.2.2 Overlap function for pulsar timing arrays

If one uses (6.9) for the Doppler frequency response of a pulsar timing measurement, then the correlation between two Earth-pulsar baseline is just a single number as the response functions

$F_{I,J}^A(\hat{k})$  are independent of frequency. This number, which can be interpreted as the expected correlation between the two pulsar timing measurement, depends on the angular separation between the two Earth-pulsar baselines. A plot of this expected correlation as a function of the angular separation between the Earth-pulsar baselines is shown in Figure 18. This is called the *Hellings-Down curve*, originally calculated in 1983 by Hellings and Down [?]. This calculation assumes that the background is unpolarized and isotropic. Generalizations of the Hellings-Down curve allowing for anisotropy and non-general-relativity polarization modes can be found in e.g., [?, ?]. The quadrupolar nature of GWs in general relativity is apparent in the Hellings-Down curve, with an angular dependence that is qualitatively similar to  $\cos(2\zeta)$ , where  $\zeta$  is the angle between two Earth-pulsar baselines.

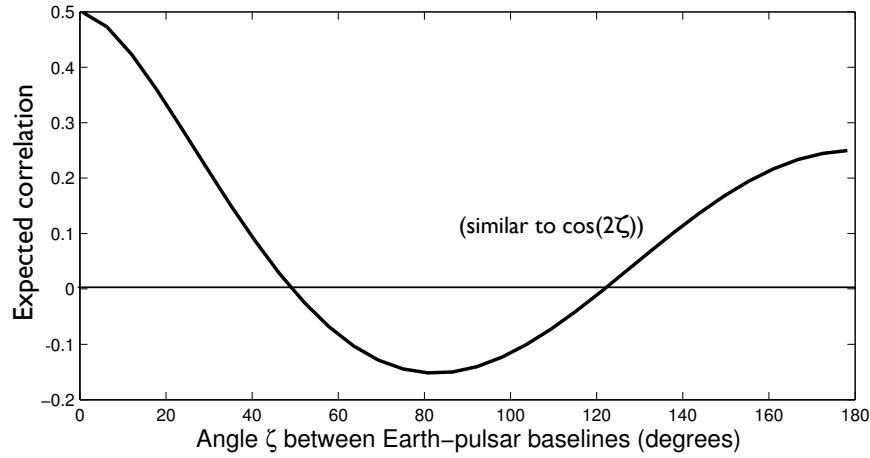


Figure 18: Hellings-Down curve. The values of the expected correlation for an unpolarized, isotropic GWB as a function of the angle  $\zeta$  between two Earth-pulsar baselines.

### 7.2.3 Overlap function for a pair of electric dipole antennas

For practice, you are asked in Exercise 7 to calculate the

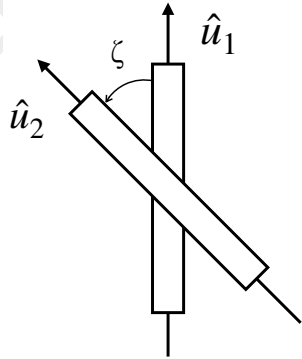


Figure 19: Geometry for calculating the overlap function for a pair of short, electric dipole antennae, for an unpolarized and isotropic electric field (Exercise 7).

## 8 What to do in the absence of correlations?

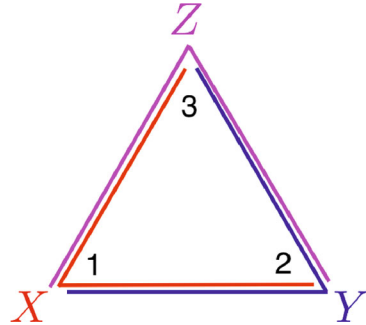


Figure 20: Schematic representation of the LISA constellation.  $X, Y, Z$  correspond to Michelson interferometers with  $60^\circ$  opening angles between the arms, with vertices located at spacecraft 1, 2, 3. From  $X, Y, Z$ , one can construct the TDI combinations  $A, E, T$  described in the text.

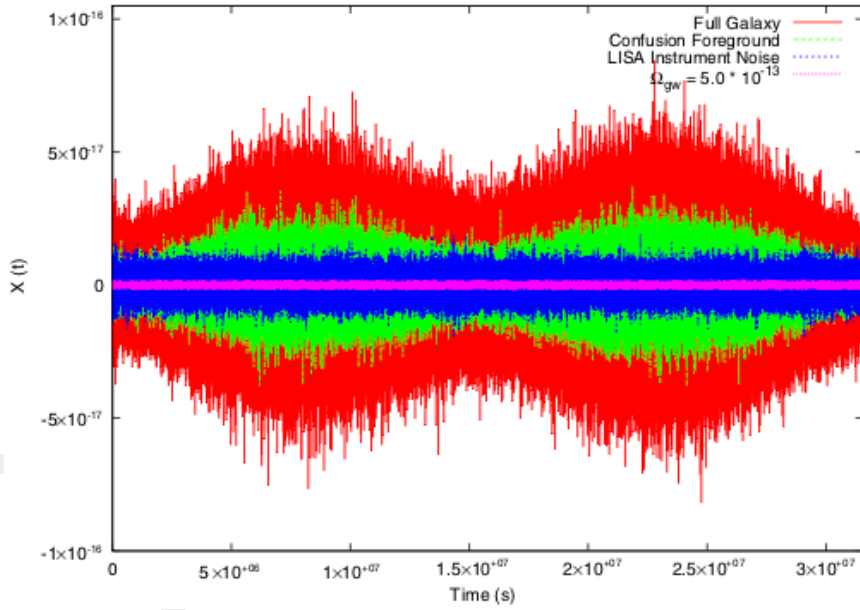


Figure 21: One-years worth of simulated timeseries data for LISA. The total output consists of a cosmological GWB (pink); LISA instrument noise (blue); the full astrophysical foreground signal from the galactic white-dwarf binary population (red), which consist of individually resolvable binary signal and the confusion-limited foreground (green). Of particular note are the amplitude and time variability of the astrophysical foreground, having a period of 6 months. Figure taken from [?].

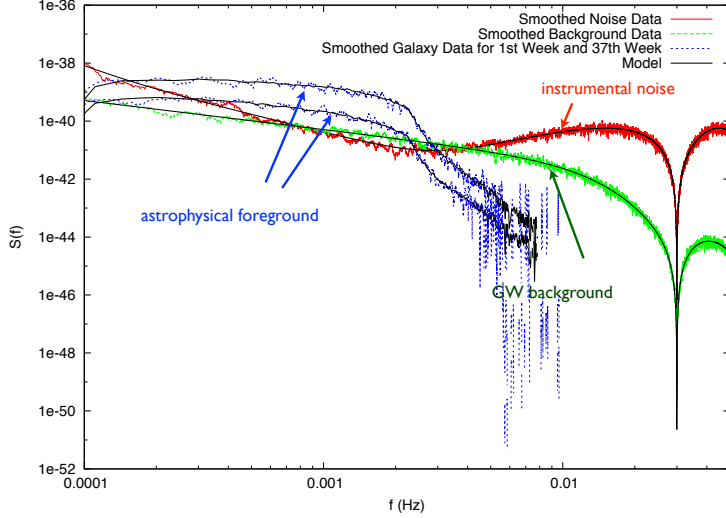


Figure 22: Simulated power spectral densities for the LISA instrumental noise (red), cosmological GWB (green) and astrophysical foreground from galactic white dwarf binaries (blue), the latter at two times during LISAs orbit. Note the strength of the astrophysical foreground relative to the instrumental noise, and the different spectral shapes for the three different contributions. Figure taken from [?].

## 9 Frequentist statistics and Bayesian inference

Bayes' theorem:

$$p(H|d) = \frac{p(d|H)p(H)}{p(d)} \quad (9.1)$$

Posterior distributions:

$$p(S_{n_1}, S_{n_2}, S_h|d, \mathcal{M}_1) = \frac{p(d|S_{n_1}, S_{n_2}, S_h, \mathcal{M}_1)p(S_{n_1}, S_{n_2}, S_h|\mathcal{M}_1)}{p(d|\mathcal{M}_1)} \quad (9.2)$$

$$p(S_h|d, \mathcal{M}_1) = \int dS_{n_1} \int dS_{n_2} p(S_{n_1}, S_{n_2}, S_h|d, \mathcal{M}_1) \quad (9.3)$$

Model selection:

$$\frac{p(\mathcal{M}_1|d)}{p(\mathcal{M}_0|d)} = \frac{p(d|\mathcal{M}_1)p(\mathcal{M}_1)}{p(d|\mathcal{M}_0)p(\mathcal{M}_0)} \quad (9.4)$$

Relationship between Bayesian and frequentist approaches:

$$\mathcal{B}_{10}(d) \equiv \frac{p(d|\mathcal{M}_1)}{p(d|\mathcal{M}_0)} = \frac{\int d\vec{\theta}_n \int d\vec{\theta}_h p(d|\vec{\theta}_n, \vec{\theta}_h, \mathcal{M}_1)p(\vec{\theta}_n, \vec{\theta}_h|\mathcal{M}_1)}{\int d\vec{\theta}_n p(d|\vec{\theta}_n, \mathcal{M}_0)p(\vec{\theta}_n|\mathcal{M}_0)} \simeq \Lambda_{\text{ML}}(d) \frac{\Delta V_1/V_1}{\Delta V_0/V_0} \quad (9.5)$$

$$(9.6)$$

$$(9.7)$$

$$(9.8)$$

(9.9)

(9.10)

(9.11)

(9.12)

(9.13)

(9.14)

(9.15)

(9.16)

(9.17)

(9.18)

(9.19)

(9.20)

(9.21)

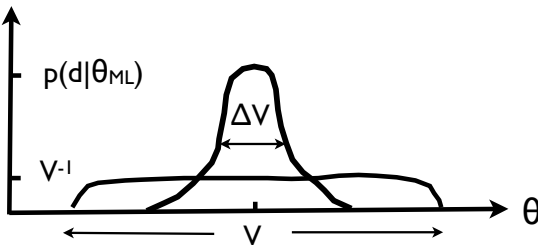


Figure 23: Schematic representation of the likelihood function and prior probability distribution for a parameter  $\theta$ , when the data  $d$  are informative. In this case, the likelihood function is peaked relative to the prior probability distribution, with maximum at  $\theta = \theta_{ML}$  and characteristic width  $\Delta V$ . The parameter space volume is denoted by  $V$ .

## 10 Searching for the background of binary black-hole mergers

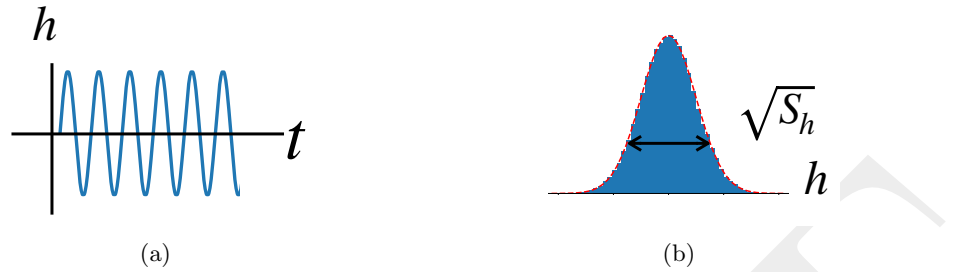


Figure 24: Different signal priors for  $h(t)$ . Panel (a): Deterministic (sinusoid) signal prior. Panel (b): Stochastic signal prior. For the stochastic signal prior,  $h(t)$  values are drawn from a Gaussian distribution with variance  $S_h$ .



Figure 25: The two components of the “mixture” signal prior for the Bayesian BBH search. Panel (a): With probability  $\xi$ , the signal prior for  $h(t)$  is a chirp waveform. Panel (b): With probability  $(1 - \xi)$ , the signal prior for  $h(t)$  is that the signal is absent, i.e.,  $h(t) = 0$ .

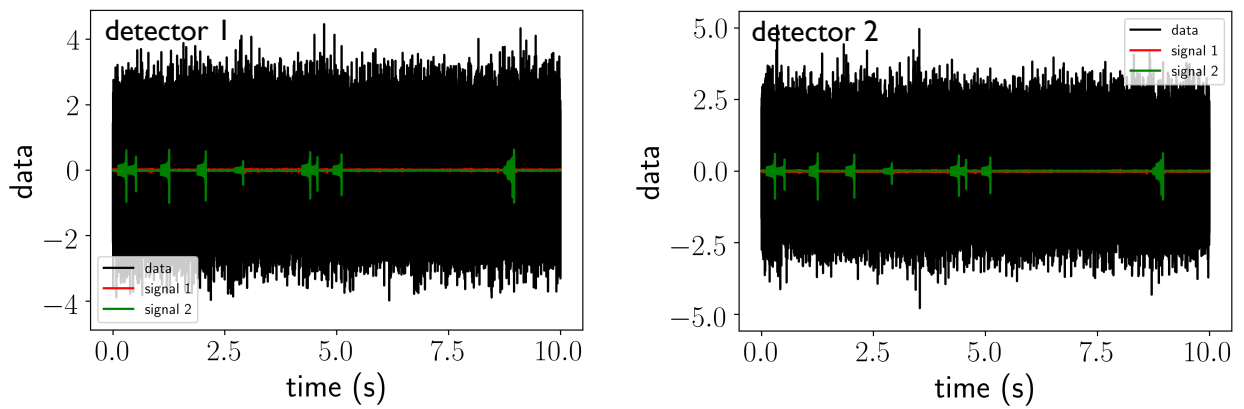


Figure 26: Simulated BBH and BNS data in two coincident and coaligned detectors. The confusion-limited BNS background is shown in orange; the popcorn-like BBH background is shown in green. The black trace is the data consisting of the BBH and BNS signal plus white Gaussian-stationary noise, uncorrelated in the two detectors.

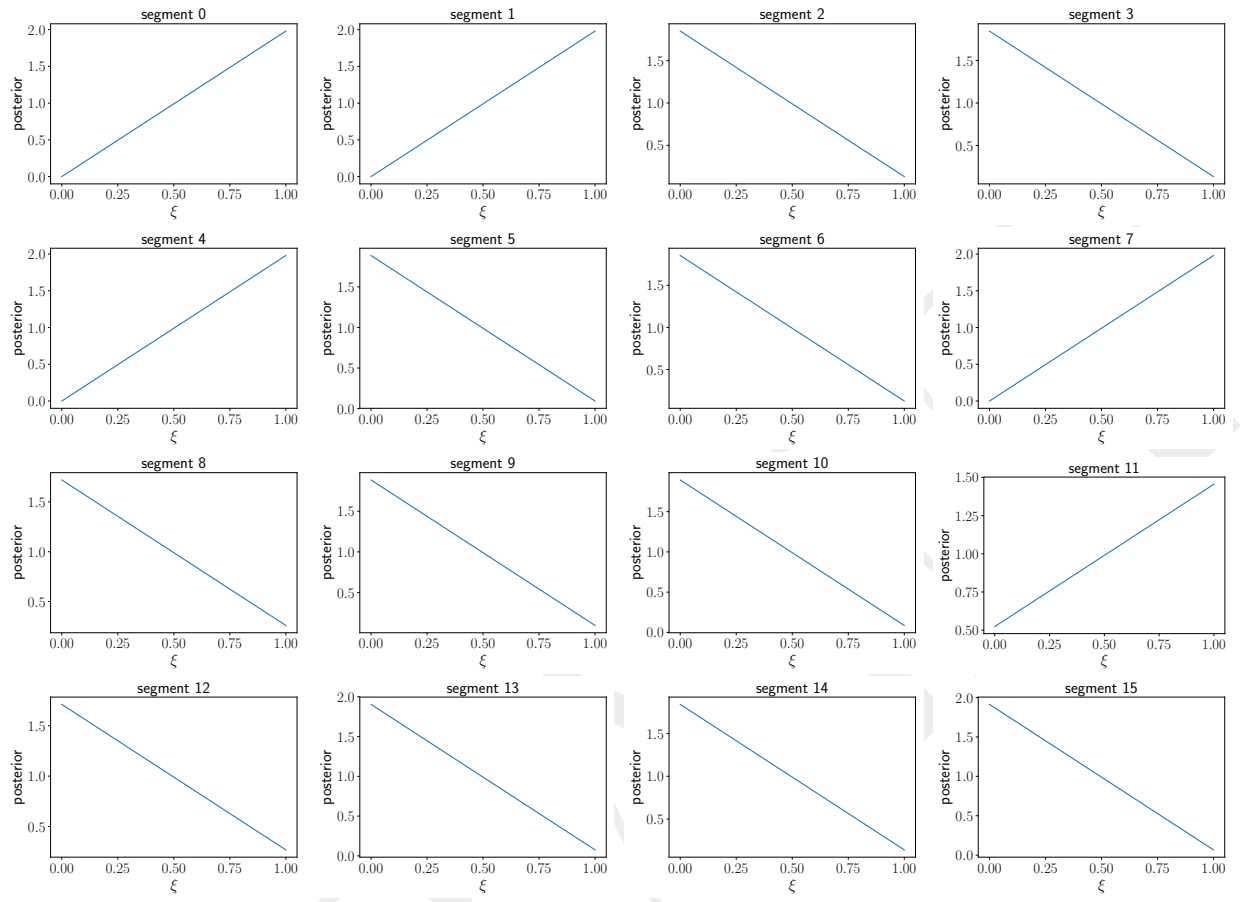


Figure 27: Posterior distributions for  $\xi$  for the first 16 segments (i.e., first 4 s) of data.

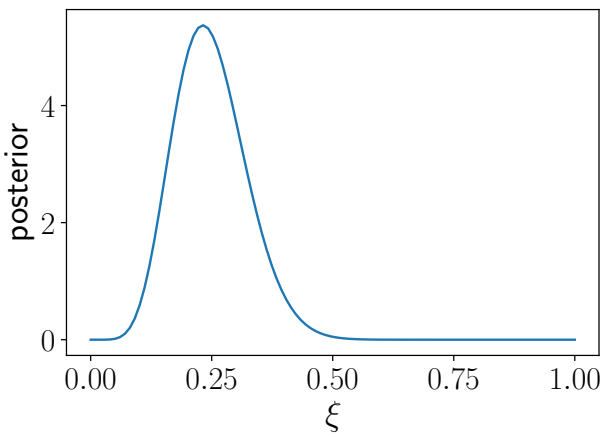


Figure 28: The cumulative posterior distribution for  $\xi$  after combining all 40 segments of data.

FREQUENTIST STATISTICS	BAYESIAN INFERENCE
probabilities are long-run relative occurrence of outcomes of repeatable experiments (i.e., random variables); cannot be assigned to hypotheses or parameters, which have fixed but unknown values	probabilities are degree of belief (or confidence) in any proposition, and hence can be assigned to hypotheses and parameters
usually start with a likelihood function $p(d H)$ , which is the probability distribution for the measured data $d$ , assuming the truth of a particular hypothesis $H$	same as frequentist approach
construct statistics for parameter estimation and hypothesis testing	specify prior degree of belief for parameters and hypotheses
calculate the probability distribution of the statistic (e.g., using time slides)	use Bayes' theorem to update degree of belief in light of new data
construct confidence intervals and $p$ -values	construct posteriors and odds ratios (Bayes factors)

Table 1: Comparison of frequentist and Bayesian approaches to statistical inference.

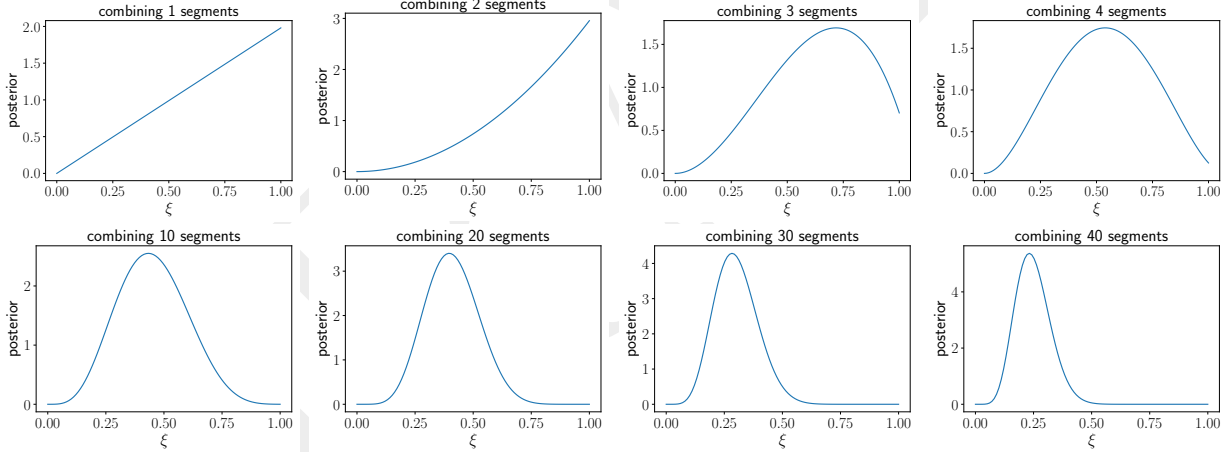


Figure 29: Cumulative posterior distributions for  $\xi$  combining the first  $n$  segments of data. The bottom-rightmost plot is also shown in Figure 28.

## 11 Exercises

### 1. Rate estimate of stellar-mass binary black hole mergers:

Estimate the total rate (number of events per time) of stellar-mass binary black hole mergers throughout the universe by multiplying LIGO's O1 local rate estimate  $R_0 \sim 10 - 200 \text{ Gpc}^{-3} \text{ yr}^{-1}$  by the comoving volume out to some large redshift, e.g.,  $z = 10$ . (For this calculation you can ignore any dependence of the rate density with redshift.) You should find a merger rate of  $\sim 1$  per minute to a few per hour.

*Hint:* You will need to do numerically evaluate the following integral for proper distance

today as a function of source redshift:

$$d_0(z) = \frac{c}{H_0} \int_0^z \frac{dz'}{E(z')} , \quad E(z) \equiv \sqrt{\Omega_m(1+z)^3 + \Omega_\Lambda} , \quad (11.1)$$

with

$$\Omega_m = 0.31 , \quad \Omega_\Lambda = 0.69 , \quad H_0 = 68 \text{ km s}^{-1} \text{ Mpc}^{-1} . \quad (11.2)$$

Doing that integral, you should find what's shown in Figure 30, which you can then evaluate at  $z = 10$  to convert  $R_0$  (number of events per comoving volume per time) to total rate (number of events per time) for sources out to redshift  $z = 10$ .

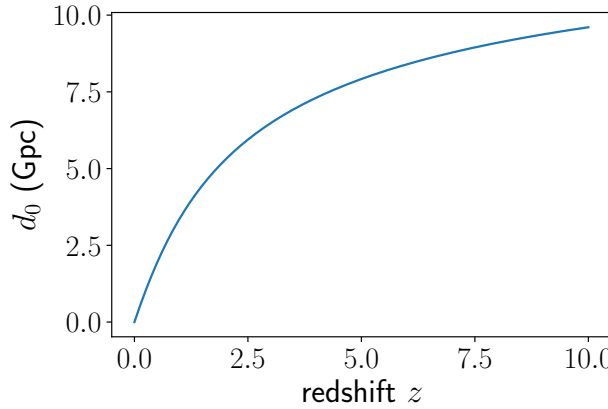


Figure 30

## 2. Relating $S_h(f)$ and $\Omega_{\text{gw}}(f)$ :

Derive the relationship

$$S_h(f) = \frac{3H_0^2}{2\pi^2} \frac{\Omega_{\text{gw}}(f)}{f^3} \quad (11.3)$$

between the strain power spectral density  $S_h(f)$  and the dimensionless fractional energy density spectrum  $\Omega_{\text{gw}}(f)$ . (*Hint:* You will need to use the various definitions of these quantities and also

$$\rho_{\text{gw}} = \frac{c^2}{32\pi G} \langle \dot{h}_{ab}(t, \vec{x}) \dot{h}^{ab}(t, \vec{x}) \rangle , \quad (11.4)$$

which expresses the energy-density in gravitational-waves to the metric perturbations  $h_{ab}(t, \vec{x})$ .)

## 3. Cosmology and the “Phinney formula” for astrophysical backgrounds:

(a) Using the Friedmann equation

$$\left( \frac{\dot{a}}{a} \right)^2 = H_0^2 \left( \frac{\Omega_m}{a^3} + \Omega_\Lambda \right) \quad (11.5)$$

for a spatially-flat FRW spacetime with matter and cosmological constant, and the relationship

$$1 + z = \frac{1}{a(t)} , \quad a(t_0) \equiv 1 \quad (t_0 \equiv \text{today}) , \quad (11.6)$$

between redshift  $z$  and scale factor  $a(t)$ , derive

$$\frac{dt}{dz} = -\frac{1}{(1+z)H_0E(z)}, \quad E(z) = \sqrt{\Omega_m(1+z)^3 + \Omega_\Lambda}. \quad (11.7)$$

(b) Using this result for  $dt/dz$ , show that

$$\Omega_{\text{gw}}(f) = \frac{f}{\rho_c H_0} \int_0^\infty dz R(z) \frac{1}{(1+z)E(z)} \left( \frac{dE_{\text{gw}}}{df_s} \right) \Big|_{f_s=f(1+z)} \quad (11.8)$$

in terms of the rate density  $R(z)$  as measured in the source frame (number of events per comoving volume per time interval in the source frame). (*Hint:* The expression for  $dt/dz$  from part (a) will allow you to go from the ‘‘Phinney formula’’ for  $\Omega_{\text{gw}}(f)$  written in terms of the number density  $n(z)$ ,

$$\Omega_{\text{gw}}(f) = \frac{1}{\rho_c} \int_0^\infty dz n(z) \frac{1}{1+z} \left( f_s \frac{dE_{\text{gw}}}{df_s} \right) \Big|_{f_s=f(1+z)}, \quad (11.9)$$

to one in terms of the rate density  $R(z)$ , where  $n(z) dz = R(z) |dt|_{t=t(z)}$ . Note: Both of the above expressions for  $\Omega_{\text{gw}}(f)$  assume that there is only one type of source, described by some set of average source parameters. If there is more than one type of source, one must sum the contributions of each source to  $\Omega_{\text{gw}}(f)$ .)

#### 4. Optimal filtering for the cross-correlation statistic:

Verify the form

$$\tilde{Q}(f) \propto \frac{\Gamma_{12}(f)H(f)}{P_1(f)P_2(f)}, \quad (11.10)$$

of the optimal filter function in the weak-signal limit, where  $H(f)$  is the assumed spectral shape of the gravitational-wave background,  $\Gamma_{12}(f)$  is the overlap function, and  $P_1(f)$ ,  $P_2(f)$  are the power spectral densities of the outputs of the two detectors (which are approximately equal to  $P_{n_1}(f)$ ,  $P_{n_2}(f)$ , respectively). Recall that the optimal filter  $\tilde{Q}(f)$  maximizes the signal-to-noise ratio of the cross-correlation statistic. (*Hint:* Introduce an inner product on the space of functions of frequency  $A(f)$ ,  $B(f)$ :

$$(A, B) \equiv \int df A(f)B^*(f)P_1(f)P_2(f). \quad (11.11)$$

This inner product has all of the properties of the familiar dot product of vectors in 3-dimensional space. The signal-to-noise ratio of the cross-correlation statistic can be written in terms of this inner product.)

#### 5. Maximum-likelihood estimators for single and multiple parameters:

(a) Show that the maximum-likelihood estimator  $\hat{a}$  of the single parameter  $a$  in the likelihood function

$$p(d|a, \sigma) \propto \exp \left[ -\frac{1}{2} \sum_{i=1}^N \frac{(d_i - a)^2}{\sigma_i^2} \right] \quad (11.12)$$

is given by the noise-weighted average

$$\hat{a} = \sum_i \frac{d_i}{\sigma_i^2} \Big/ \sum_j \frac{1}{\sigma_j^2}. \quad (11.13)$$

(b) Extend the previous calculation to the likelihood

$$p(d|A, C) \propto \exp \left[ -\frac{1}{2}(d - MA)^\dagger C^{-1}(d - MA) \right], \quad (11.14)$$

where  $A \equiv A_\alpha$  is a vector of parameters,  $C \equiv C_{ij}$  is the noise covariance matrix, and  $M \equiv M_{i\alpha}$  is the response matrix mapping  $A_\alpha$  to data samples,  $MA \equiv \sum_\alpha M_{i\alpha} A_\alpha$ . For this more general case you should find:

$$\hat{A} = F^{-1}X, \quad (11.15)$$

where

$$F \equiv M^\dagger C^{-1} M, \quad X \equiv M^\dagger C^{-1} d. \quad (11.16)$$

In general, the matrix  $F$  (called the *Fisher* matrix) is not invertible, so some sort of regularization is needed to do the matrix inversion.

#### 6. Timing-residual response for a 1-arm, 1-way detector:

Derive the timing residual response function

$$R^A(f, \hat{k}) = \frac{1}{2} u^a u^b e_{ab}^A(\hat{k}) \frac{1}{i2\pi f} \frac{1}{1 - \hat{k} \cdot \hat{u}} \left[ 1 - e^{-\frac{i2\pi f L}{c}(1 - \hat{k} \cdot \hat{u})} \right] \quad (11.17)$$

for a single-link (i.e., a one-arm, one-way detector like that for pulsar timing). Here  $\hat{u}$  is the direction of propagation of the electromagnetic pulse, and  $\hat{k}$  is the direction of propagation of the GW (the direction to the GW source is  $\hat{n} \equiv -\hat{k}$ , and the direction to the pulsar is  $\hat{p} \equiv -\hat{u}$ ). The origin of coordinates is taken to be at the position of the detector.

#### 7. Overlap function for colocated electric dipole antennae:

Show that the overlap function for a pair of (short) colocated electric dipole antennae pointing in directions  $\hat{u}_1$  and  $\hat{u}_2$  (Figure 19) is given by

$$\Gamma_{12} \propto \hat{u}_1 \cdot \hat{u}_2 \equiv \cos \zeta \quad (11.18)$$

for the case of an unpolarized, isotropic electromagnetic field. (*Hint:* “short” means that the phase of the electric field can be taken to be constant over the lengths of the dipole antennae, so that the response of antenna  $I = 1, 2$  to the field is given by  $r_I(t) = \hat{u}_I \cdot \vec{E}(t, \vec{x}_0)$ , where  $\vec{x}_0$  is the common location of the two antennae.)

#### 8. Maximum-likelihood estimators for the standard cross-correlation statistic:

Verify that

$$\hat{C}_{11} \equiv \frac{1}{N} \sum_{i=1}^N d_{1i}^2, \quad \hat{C}_{22} \equiv \frac{1}{N} \sum_{i=1}^N d_{2i}^2, \quad \hat{C}_{12} \equiv \frac{1}{N} \sum_{i=1}^N d_{1i} d_{2i} \quad (11.19)$$

are maximum-likelihood estimators of

$$S_1 \equiv S_{n_1} + S_h, \quad S_2 \equiv S_{n_2} + S_h, \quad S_h, \quad (11.20)$$

for the case of  $N$  samples of a white GWB in uncorrelated white detector noise, for a pair of colocated and coaligned detectors. Recall that the likelihood function is

$$p(d|S_{n_1}, S_{n_2}, S_h) = \frac{1}{\sqrt{\det(2\pi C)}} \exp \left[ -\frac{1}{2} d^T C^{-1} d \right], \quad (11.21)$$

where

$$C = \begin{bmatrix} (S_{n_1} + S_h) \mathbf{1}_{N \times N} & S_h \mathbf{1}_{N \times N} \\ S_h \mathbf{1}_{N \times N} & (S_{n_2} + S_h) \mathbf{1}_{N \times N} \end{bmatrix} \quad (11.22)$$

and

$$d^T C^{-1} d \equiv \sum_{I,J=1}^2 \sum_{i,j=1}^N d_{Ii} (C^{-1})_{Ii,Jj} d_{Jj}. \quad (11.23)$$

#### 9. Derivation of the maximum-likelihood ratio detection statistic:

Verify that twice the log of the maximum-likelihood ratio for the standard stochastic likelihood function goes like the square of the (power) signal-to-noise ratio,

$$2 \ln \Lambda_{\text{ML}}(d) \simeq \frac{\hat{C}_{12}^2}{\hat{C}_{11}\hat{C}_{22}/N}, \quad (11.24)$$

in the weak-signal approximation. (*Hint:* For simplicity, do the calculation in the context of  $N$  samples of a white GWB in uncorrelated white detector noise, for a pair of colocated and coaligned detectors, using the results of Exercise 8.)

#### 10. Standard cross-correlation likelihood by marginalizing over stochastic signal prior:

Derive the standard form of the likelihood function for stochastic background searches

$$p(d|S_{n_1}, S_{n_2}, S_h) = \frac{1}{\sqrt{\det(2\pi C)}} \exp \left[ -\frac{1}{2} \sum_{I,J=1}^2 d_I (C^{-1})_{IJ} d_J \right], \quad (11.25)$$

where

$$C \equiv \begin{bmatrix} S_{n_1} + S_h & S_h \\ S_h & S_{n_2} + S_h \end{bmatrix}, \quad (11.26)$$

by marginalizing

$$p_n(d - h|S_{n_1}, S_{n_2}) = \frac{1}{2\pi\sqrt{S_{n_1}S_{n_2}}} \exp \left[ -\frac{1}{2} \left\{ \frac{(d_1 - h)^2}{S_{n_1}} + \frac{(d_2 - h)^2}{S_{n_2}} \right\} \right] \quad (11.27)$$

over the signal samples  $h$  for the *stochastic* signal prior

$$p(h|S_h) = \frac{1}{\sqrt{2\pi S_h}} \exp \left[ -\frac{1}{2} \frac{h^2}{S_h} \right]. \quad (11.28)$$

In other words, show that

$$p(d|S_{n_1}, S_{n_2}, S_h) = \int_{-\infty}^{\infty} dh p_n(d - h|S_{n_1}, S_{n_2}) p(h|S_h). \quad (11.29)$$

(*Hint:* You'll have to complete the square in the argument of the exponential in the marginalization integral.)

## References

- [1] Phinney, E.S., “A practical theorem on gravitational wave backgrounds” (2001). [arXiv:0108028 [astro-ph.IM]].
- [2] Romano, Joseph D. and Cornish, Neil. J., “Detection methods for stochastic gravitational-wave backgrounds: a unified treatment”, *Living Reviews in Relativity*, **20**(1), 2 (Apr 04, 2017). [DOI]URL:  
<https://doi.org/10.1007/s41114-017-0004-1>.
- [3] Smith, Rory and Thrane, Eric, “Optimal Search for an Astrophysical Gravitational-Wave Background”, *Phys. Rev. X*, **8**, 021019 (Apr 2018). [DOI]URL:  
<https://link.aps.org/doi/10.1103/PhysRevX.8.021019>.